

Polymer-Sulfide Composite Solid Electrolytes: Design, Interfacial Engineering, and Performance Optimization for All-Solid-State Lithium-Ion Batteries

Yajuan Zhang, Ying Yin, Peng Sun, Xi Zhang,* and Jinliang Li*

Driven by the dual demands for high energy density and intrinsic safety in next-generation power systems, all-solid-state lithium-ion batteries (ASSLIBs) using nonflammable solid-state electrolytes have garnered significant attention. Among the candidates, sulfide-based solid electrolytes (SSEs) are particularly promising due to their high ionic conductivity and soft mechanical properties. However, challenges such as their sensitivity to moisture and oxygen, electrochemical instability, and poor interfacial contact with electrodes hinder their practical application. To address these bottlenecks, this review highlights recent advances in material design and interfacial engineering of sulfide-incorporated polymer matrix and summarizes how the introduction of sulfides into

binders, gel polymers, and related systems improves interfacial electrochemical properties in ASSLIBs, along with the underlying mechanisms governing their electrochemical performance. In addition, we provide an in-depth discussion of how embedding sulfide solid electrolytes into polymer matrix enables the construction of 3D ion transport networks, elucidating how interfacial energy barrier modulation and space-charge layer formation enhance electrochemical stability and how multilayer barrier architectures contribute to improved environmental tolerance. We believe that our work will provide both theoretical insights and a technological roadmap for the development of high-performance ASSLIBs.

1. Introduction

The pursuit of both high energy density and robust safety in electric vehicles and large-scale energy storage systems has highlighted the intrinsic limitations of conventional liquid lithium-ion batteries (LIBs).^[1–3] Organic liquid electrolytes, while enabling fast ion transport, are inherently flammable and volatile, creating persistent risks of thermal runaway and raising serious concerns for system-level safety.^[4] In addition, the use of advanced electrode chemistries, such as silicon anodes and high-nickel cathodes, is significantly constrained by the narrow electrochemical stability window of liquid electrolytes. Severe side reactions at the electrode-electrolyte interface further accelerate performance degradation, ultimately restricting advances in energy density.^[5,6]

All-solid-state lithium ion batteries (ASSLIBs) have emerged as a compelling alternative by replacing liquid electrolytes with solid-state electrolytes (SSEs). This design eliminates the hazards of leakage and combustion, while at the same time enabling the integration of Li metal anodes (theoretical capacity: 3860 mAh g⁻¹) with high-voltage cathodes (>4.5 V).^[7,8] Such pairings promise gravimetric energy densities beyond 500 Wh kg⁻¹, positioning ASSLIBs as a next-generation solution for both mobility and stationary storage.^[9–11] Within the diverse family of SSEs, sulfide-based electrolytes are particularly attractive because of their liquid-like ion transport and outstanding room-temperature ionic conductivities.^[12,13] These properties originate from the fundamental characteristics of sulfide anions (S²⁻): their larger ionic radius and lower electronegativity compared to O²⁻ result in weaker Li-ion binding and reduced lattice distortion, while their strong polarizability diminishes Coulombic interactions, collectively enhancing Li-ion mobility.^[14,15] Sulfide electrolytes also combine a wide electrochemical stability window (>5 V) with favorable mechanical softness, allowing facile densification by cold pressing and promoting intimate electrode-electrolyte interfacial contact in bulk-type cells.^[16,17] Despite these advantages, practical implementation remains hindered by several intrinsic challenges. Sulfide electrolytes are extremely sensitive to air and moisture, necessitating strict protection during synthesis and handling.^[18,19] Their electrochemical stability is also problematic: phosphorus and germanium centers tend to be reduced by Li metal, while sulfide anions undergo oxidation at high voltages.^[20,21] Direct contact with Li further exacerbates interfacial degradation, leading to resistive interphase formation. Moreover, although mechanically softer than oxides, sulfides still require significant stack pressure to maintain effective

Y. Zhang, X. Zhang
School of Mechanical Engineering
Shanghai Jiao Tong University
Shanghai 200240, P. R. China
E-mail: braver1980@sjtu.edu.cn

Y. Yin
Shenzhen Automotive Research Institute
Beijing Institute of Technology
Shenzhen, Guangdong 518118, China

P. Sun, J. Li
Siyuan Laboratory
Guangdong Provincial Engineering Technology Research Center of Vacuum Coating Technologies and New Energy Materials
Department of Physics
College of Physics & Optoelectronic Engineering
Jinan University
Guangzhou 510632, P. R. China
E-mail: lijinliang@email.jnu.edu.cn

solid-solid interfacial contact, posing additional barriers to large-scale integration.

Meeting the diverse performance requirements of ASSLIBs remains one of the most formidable obstacles in next-generation energy storage. Polymer electrolytes such as polyethylene oxide (PEO) and polyacrylonitrile (PAN) are attractive for their interfacial compatibility and ease of processing, yet their room-temperature ionic conductivities typically fall below $10^{-5} \text{ S cm}^{-1}$, and their mechanical strength is inadequate to prevent Li dendrite growth.^[22,23] Sulfide electrolytes, in contrast, deliver liquid-like conductivities ($>10^{-3} \text{ S cm}^{-1}$) and favorable interfacial contact after cold pressing but suffer from poor air stability, electrochemical reactivity with Li metal, and the need for high stack pressure.^[24,25] No single electrolyte system can therefore reconcile the combined demands of conductivity, mechanical robustness, stability, and environmental tolerance required for commercial deployment.

A promising pathway lies in hybridizing polymers with sulfide electrolytes to create to obtain polymer-sulfide composite solid electrolytes (PSCSEs) that combine the strengths of both components.^[26,27] In these bicontinuous architectures, sulfide fillers such as $\text{Li}_6\text{PS}_5\text{Cl}$ or $\text{Li}_{10}\text{GeP}_2\text{S}_{12}$ establish percolating ion-conduction networks, while polymer matrices, including thermoplastic polyamides or chemically crosslinked PEO, offer elasticity in the 0.1–1 GPa range to accommodate interfacial stress and encapsulate fragile sulfide domains.^[28,29] Such synergy not only boosts mechanical reliability but also markedly improves environmental stability: composite membranes typically retain over 85% of their conductivity after ambient exposure, compared to catastrophic degradation in pristine sulfides, as shown in Figure 1.^[30,31] Meanwhile, processing strategies such as hot-melt compounding and low-pressure pressing enable polymers to infiltrate sulfide agglomerates, forming continuous conduction pathways that reduce interfacial resistance.

This review highlights the groundbreaking advancements in the field of PSCSE research between 2023 and 2025. It systematically elaborates on a forward-looking conceptual framework that could shape future research. We argue that the key to unlocking the full potential of PSCSEs lies in the synergistic regulation of three interconnected factors: 1) dynamic interfacial chemistry

at the polymer–sulfide–electrode junction, 2) the design of hierarchical ion-transport networks spanning molecular to macroscopic scales, and 3) mechanical adaptability that mitigates stress accumulation and interfacial fracture. By unifying these aspects into a single framework, this work moves beyond fragmented case studies and offers a systems-level perspective. Furthermore, we propose that integrating PSCSE design with machine learning-guided material discovery and scalable low-pressure processing strategies will be pivotal for translating laboratory progress into industrial reality. We believe this work will provide theoretical guidance and a technical roadmap for the development of high-performance ASSLIBs.

2. Design of PSCSE Materials

2.1. Binder in SSE

Despite their high rigidity, SSE generally suffer from poor interfacial contact with electrode materials in ASSLIBs, leading to increased interfacial resistance and degraded cycling stability.^[32,33] In addition, their inherent brittleness and fracture tendency during processing and operation often trigger structural failure.^[34,35] To address these challenges, researchers have widely introduced polymeric binders, well established in LIBs, to construct flexible interlayers at the electrolyte-electrode interface. This “rigid-flexible integration” strategy not only improves solid–solid interfacial contact and reduces interfacial impedance but also enhances structural stability and processability.^[36,37] Polymeric binders simultaneously act as an adhesive matrix, bonding electrolyte particles into a mechanically coherent film, while imparting bendability and roll-to-roll compatibility to accommodate volume variations during long-term cycling.

Hong et al. adopted a dry-processing strategy to fabricate composite cathodes by blending $\text{Li}_6\text{PS}_5\text{Cl}$ with a Li-ion conducting ionomer binder, poly(tetrafluoroethylene-co-perfluoro(3-oxa-4-pentene sulfonic acid) lithium salt) (ionomer).^[38] This ionomer not only enhanced Li^+ transport but also ensured intimate contact

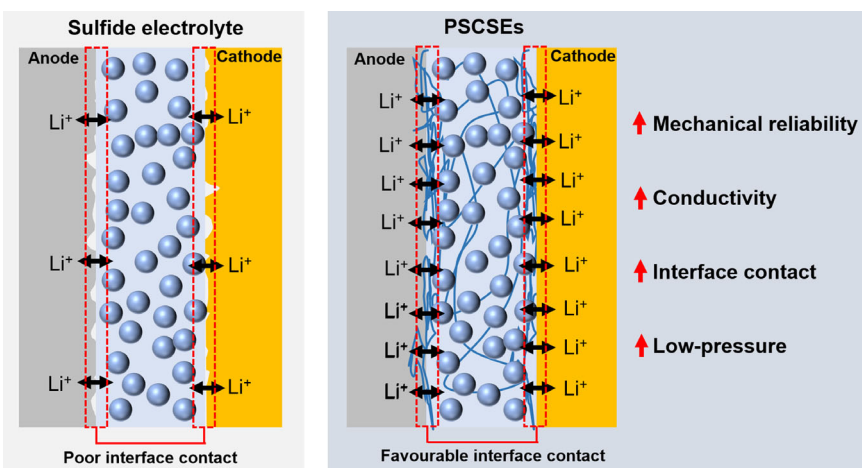


Figure 1. Schematic of the PSCSEs' advantages.

among $\text{LiNi}_{0.7}\text{Co}_{0.1}\text{Mn}_{0.2}\text{O}_2$ (NCM712), conductive carbon, and the solid electrolyte, thereby achieving a high capacity of 180.7 mAh g^{-1} at 0.1 C and 90% retention after 300 cycles at 0.5 C . Surface and interfacial cutting analysis (SAICAS) (Figure 2a–c) confirmed superior horizontal and vertical adhesion relative to polytetrafluoroethylene (PTFE), while nanoindentation revealed a higher elastic recovery ratio (0.66 vs. 0.47), effectively buffering active material volume changes and contributing to long-term stability. Expanding the role of elastic binders, Oh et al. incorporated spandex into sulfide-based protective layers for Ag-C composites (Figure 2d).^[39] The hard urethane/MDI/urea/EDA segments conferred structural rigidity, whereas soft poly(ethylene glycol) (PEG) chains imparted elasticity and stretch, recovery. Strong hydrogen bonding between polar substituents and Ag surface hydroxyls promoted uniform dispersion and adhesion, suppressing Li trapping and irreversible capacity loss, thereby improving reversibility in anode-free ASSLIBs. In parallel, Liu et al. fabricated flexible composite electrolytes via electrospinning-impregnation-hot-pressing, combining $\text{Li}_6\text{PS}_5\text{Cl}$ with polar poly(vinylidene fluoride-co-trifluoroethylene) (P(VDF-TrFE)) binder.^[40] The high dielectric constant and viscoelasticity of P(VDF-TrFE) enabled the formation of a self-supporting porous scaffold (10–20 μm pore size) after electrospinning, which allowed uniform infiltration of sulfide particles. At an optimized composition (79:21 wt % $\text{Li}_6\text{PS}_5\text{Cl}$:P(VDF-TrFE)), the composite membrane exhibited high ionic conductivity ($\approx 1.2 \text{ mS cm}^{-1}$) and mechanical flexibility. When paired with LiNbO_3 -coated $\text{LiNi}_{0.8}\text{Co}_{0.1}\text{Mn}_{0.1}\text{O}_2$ (NCM811)

cathodes and Li-In anodes, 30–40 μm -thick membranes delivered 92% capacity retention after 1000 cycles at 1.61 C and stable cycling up to 20 000 cycles. Nevertheless, the aforementioned SSEs still exhibit poor compatibility with the cathode, leading to significant capacity and voltage degradation at higher current densities.

To address binder-SSE incompatibility, Kim et al. introduced a co-solvent strategy using volatile ethyl acetate and less-volatile hexyl butyrate, effectively suppressing polyvinylidene fluoride hexafluoropropylene (PVDF-HFP) binder migration.^[41] As shown in Figure 2e–g, Li-ion conductivity correlated with electrochemical performance (PVDF-HFP≈Nitrile butadiene rubber (NBR) > NBR-wt), while electronic conductivity showed the opposite trend. The superior performance of PVDF-HFP-derived electrodes was attributed to its optimal volume fraction and distribution in $\text{LiNi}_{0.7}\text{Co}_{0.15}\text{Mn}_{0.15}\text{O}_2$ (NCM711), outperforming nitrile butadiene rubber (NBR) even at 0°C and 2 MPa. Pouch-cell tests with NCM711/graphite further validated its potential. To mitigate chemo-mechanical degradation in solid-state sulfur cathodes, Ren et al. proposed an in situ encapsulation approach using a polymer electrolyte coating.^[42] The engineered composite cathode integrated an LPS sulfide electrolyte, flexible polymer layer, conductive carbon-fiber framework, and elemental sulfur (Figure 2i). In contrast to conventional insulating binders that often suffer from delamination, the polymer electrolyte simultaneously provided elastic reinforcement, chemical stabilization, and enhanced cycling durability. Covalent interactions between

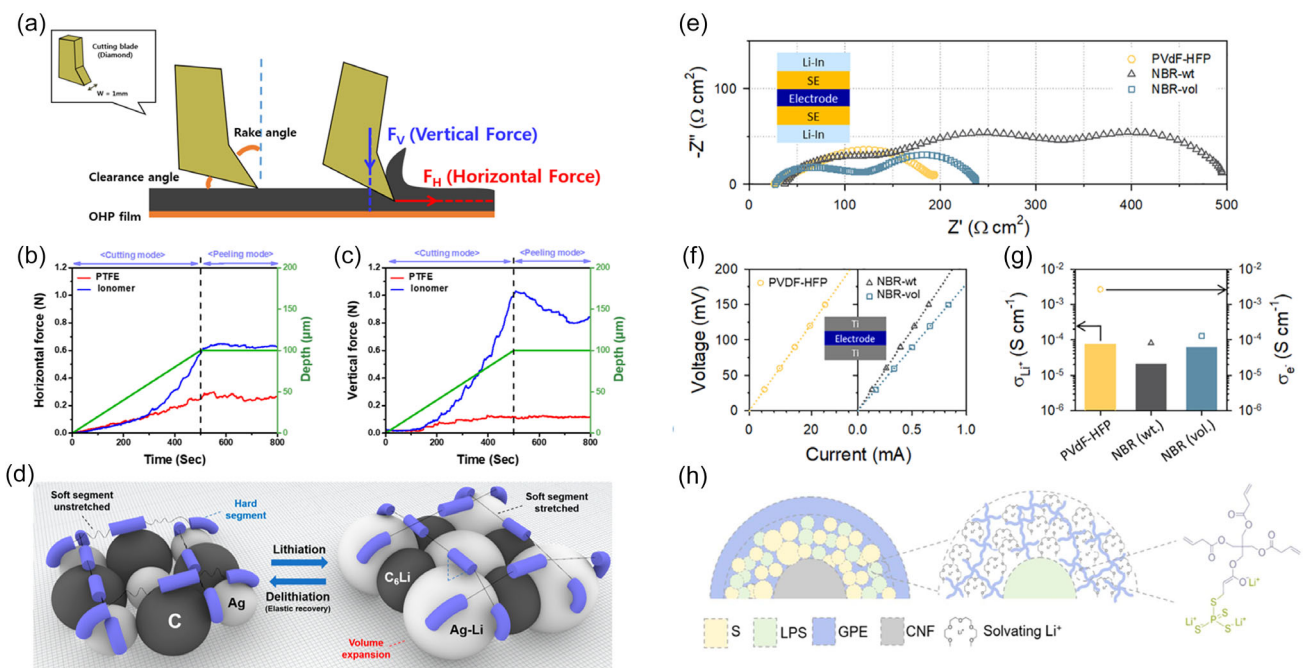


Figure 2. a) Illustration of the SAICAS experimental setup, b,c) comparison of the forces required to cut (horizontal) and peel (vertical) composite cathodes fabricated using PTFE or ionomer binders. Reproduced with permission from Ref. [38] Copyright 2022, American Chemical Society. d) 3D representation of the elastic deformation and recovery of Ag particles during lithiation and delithiation. Reproduced with permission from Ref. [39] Copyright 2022, American Chemical Society. e) Nyquist impedance spectra for electron-blocking symmetric cells configured as (Li-In)/LPSX/electrode/LPSX/Li-In, f) current-voltage curves for Li^+ -blocking Ti/electrode/Ti symmetric cells, and g) the derived Li^+ (left) and e^- (right) conductivities. Reproduced with permission from Ref. [41] Copyright 2022, Elsevier. h) Schematic depiction of electrode components, showing from left to right a fiber cross-section within the electrode, an LPS particle grafted with gel polymer electrolyte, and the crosslinked LPS/PETEA network. Reproduced with permission from Ref. [42] Copyright 2022, Springer Nature.

the polymer electrolyte and the SSE effectively suppressed parasitic interfacial reactions, while the intrinsic elasticity of the polymer electrolyte maintained intimate interfacial contact, thereby improving sulfur utilization. Benefiting from these synergistic effects, the encapsulated solid-state sulfur cathode achieved a reversible capacity of $\approx 700 \text{ mAh g}^{-1}$ with excellent retention over 100 cycles. Lee et al. systematically examined NBR binders, finding NBR25 (25 wt% AN) offered the best elasticity-adhesion balance, enabling Li-In/Li₆PS₅Cl/NCM712 full cells to reach 149 mAh g^{-1} at 0.2 C and 25 °C with stable cycling.^[43]

To simultaneously ensure mechanical robustness and interfacial stability, Li et al. engineered sulfide-based solid electrolytes into self-standing thin films using a porous poly(ethylene-co-vinyl acetate) (PEVA) scaffold combined with PTFE.^[44] Figure 3a presents the schematic depiction of Li₃N-rich SEI formation on a Li metal anode. The resulting 40 μm films exhibited high ionic conductivity (1.1 mS cm^{-1}) and tensile strength (74 MPa). An *in situ* Li₃N-rich solid electrolyte interphase (SEI) on Li effectively suppressed dendrite growth and parasitic reactions with PTFE. Galvanostatic ramp tests in Li||Li symmetric cells demonstrated that engineered Li₆PS₅Cl (E-LPSCl) films maintained stability up to 0.7 mA cm^{-2} , whereas pristine films short-circuited at 0.3 mA cm^{-2} (Figure 3b). Li-Li₃N/E-LPSCl cells achieved a critical current density of 1.0 mA cm^{-2} and cycled stably for 800 h at 0.2 mA cm^{-2} (Figure 3c). Incorporating oxidation-resistant Li₂ZrCl₅F into composite cathodes paired with E-LPSCl films yielded ASSLIBs with high energy density (354.4 Wh kg^{-1}), fast-charging capability, and excellent cycling performance.

To address limited polarity in conventional electrode slurries, Jeong et al. used poly(vinylidene fluoride-co-chlorotrifluoroethylene) (PVdF-CTFE) as a binder for NCM712||Li₆PS₅Cl||Super C composites.^[45] The polar C—F bonds facilitated intimate interfacial contact, enhancing Li⁺ transport, reducing interfacial resistance, and reinforcing mechanical integrity. Figure 3d shows the schematic of charge density distribution for different binders and their influence on adhesion and Li-ion transport within slurry-based composite cathodes. Compared with nonpolar butadiene rubber, PVdF-CTFE-based cathodes exhibited uniform microstructure and fast ion conduction, enabling ASSLIBs with Ag/C anode-free electrodes to deliver 198.5 mAh g^{-1} at 0.1 C and 74.5% retention after 300 cycles at 60 °C and 0.5 C. Similarly, Jo et al. investigated NBR binders in Si-C anodes and LiNi_{0.82}Co_{0.1}Mn_{0.08}O₂ cathodes, showing that an optimized 1.5 wt% content maximized capacity retention and rate performance, whereas excessive binder induced parasitic reactions and degraded cycling stability, as revealed by TOF-SIMS.^[46]

In oxide/sulfide hybrid systems, Kang et al. used an oxide/polymer composite electrolyte as an interfacial layer to suppress parasitic reactions while retaining sulfide electrolytes on the cathode side.^[47] Their design integrated Li₆PS₅Cl with Ag and Ge garnet-type dopants in LiNi_{0.4}Co_{0.2}Mn_{0.4}O₂ (NCM424)||PVDF||Super-P cathodes, paired with a CSE layer of Al-doped Li₇La₃Zr₂O₁₂, PEO, and Li metal anode. A precoated LiNbO₃ layer on NCM424 mitigated side reactions, yielding 163 mAh g^{-1} at 70 °C, 0.1 C, with 83% retention after 50 cycles. Battery performance was sensitive to PVDF content and electrode drying

temperature, with plasticizers alleviating activation limitations. To investigate the growth mechanisms of dendrites under high pressure in CSE, Liu et al. conducted *in situ* visualization of dendrite propagation in Li||LPSC||LPSC-PTFE||LPSC||Cu cells under 30 MPa.^[48] The dendrites initially emerged as black spots within the LPSC-PTFE layer and progressively penetrated the LPSC layer, demonstrating distinct defect-chain-guided growth behavior. Figure 3e provides a schematic illustration of the customized visualization setup. Figure 3f displays time-lapse optical microscopy images captured through the transparent sidewall during Li deposition at 2 mA cm^{-2} . Prior to Li deposition, the cross-sectional view of the transparent Li||LPSC||LPSC-PTFE||LPSC||Cu cell under an applied pressure of 30 MPa showed a uniformly gray solid electrolyte layer under optical microscopy. After 30 min of Li deposition on the copper electrode, black spots appeared in the LPSC-PTFE layer, indicating that dendrites had penetrated the thin LPSC layer adjacent to the copper electrode. The presence of multiple black spots at the LPSC/LPSC-PTFE interface suggested multidirectional dendritic growth within the LPSC layer. As plating continued, the dark regions, representing electronic conduction pathways, extended further into the LPSC-PTFE layer. After 8 h of deposition, these electron-conducting paths, mimicking dendritic trajectories, fully penetrated the LPSC-PTFE layer and began to extend invisibly into the LPSC layer on the Li electrode side. It was found that within the CSE architecture, incorporating LiF into the LPSC matrix increased the interfacial energy, thereby effectively suppressing dendrite propagation. We also suggest that this visualization setup provides an effective approach for analyzing the formation processes of dendrites, dead lithium, and other phenomena in ASSLIBs. Furthermore, it can be extended to investigate interfacial issues in ASSLIBs, including interface cracking and stress evolution. Since the introduction of LiF into the LPSC matrix could enhance the interfacial energy and effectively inhibit the growth of dendrites, the authors discovered that this strategy enabled stable cycling of Li||LPSC-LiF||Li symmetric cells for over 1800 h at 0.5 mA cm^{-2} , while Li||LPSC-LiF||LiCoO₂ cells remained free of short circuits after 200 cycles. Regarding the compatibility of the interface, Li et al. also used PVDF as a sacrificial agent to reduce LiCoO₂ thermal treatment temperature, forming *in situ* CoO/Li₂CO₃/LiF interlayers that enhanced interfacial compatibility, enabling high-voltage operation (4.5 V) and high cathode loading. Treated LiCoO₂ exhibited 145.3 mAh g^{-1} initial capacity, with high-loading cathodes (16.63 mg cm^{-2}) delivering 1.96 mAh cm^{-2} (162.8 mAh g^{-1}) and 80.33% retention after 80 cycles.^[49] Cha et al. introduced Li-doped Nafion (Nafion-Li) as a dry-processed binder for Li₆PS₅Cl/NCM711 cathodes, achieving 177.8 mAh g^{-1} at 25 °C and 97% retention after 200 cycles by enhancing ionic/electronic conductivity and constructing a stable three-phase interfacial network.^[50]

Song et al. developed a PVDF-HFP-based composite electrolyte (LPS_x) incorporating sulfur-vacancy-rich tungsten sulfide (WS_x).^[51] The abundant sulfur vacancies interact electrostatically with PVDF-HFP chains and promote LiFSI dissociation via orbital hybridization between Li s-orbitals and S p-orbitals, generating a high concentration of free Li-ion and FSI⁻ ions, as shown in Figure 4a. This strong interaction enhances ionic conductivity

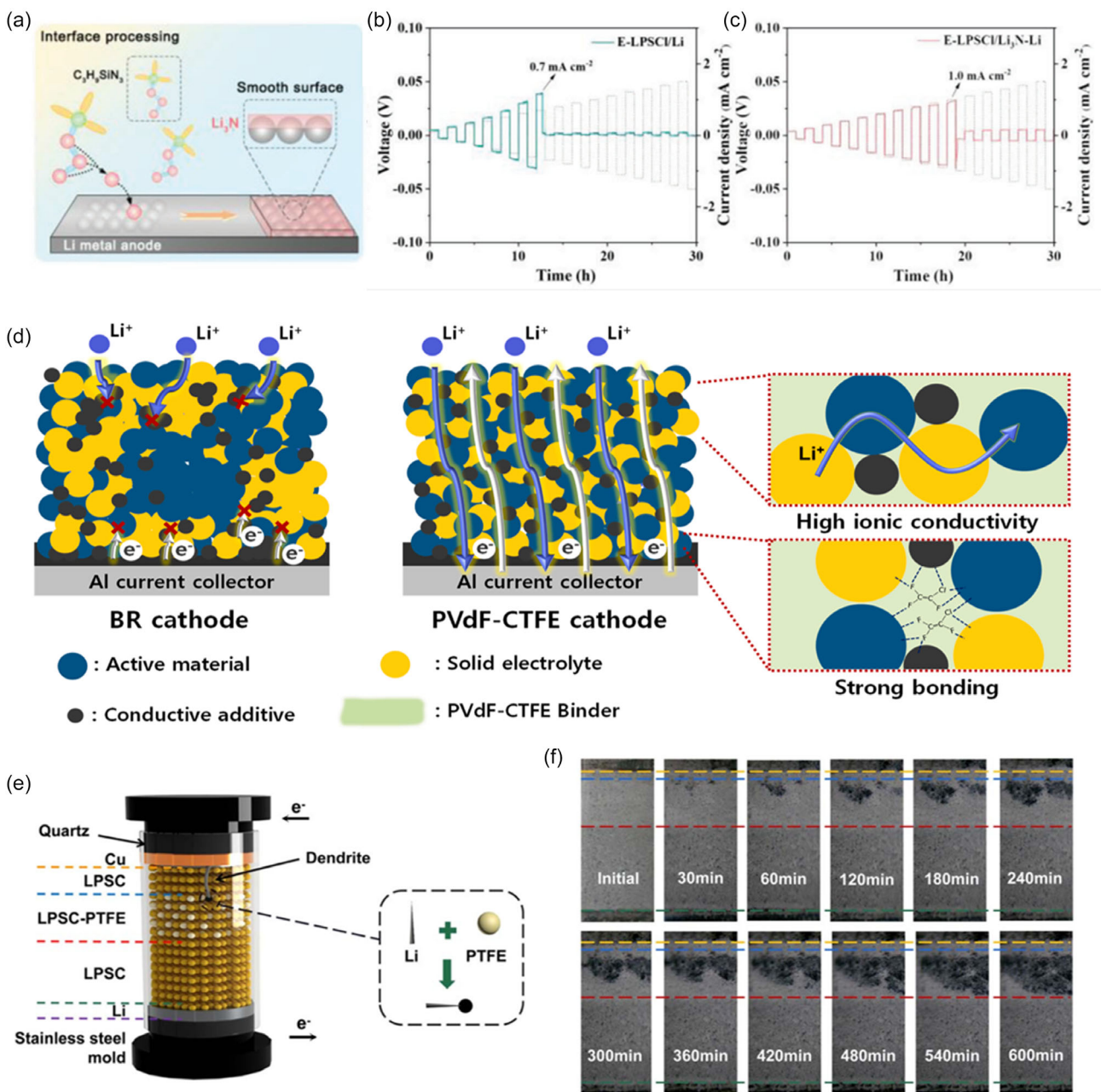


Figure 3. a) Schematic depiction of Li_3N -rich SEI formation on a Li metal anode. CCD measurements of b) E-LPSC film interfaced with pristine Li metal and c) E-LPSC film with a Li_3N -modified Li anode. Reproduced with permission from Ref. [44] Copyright 2024, Wiley. d) Illustration of charge density distribution for different binders and their influence on adhesion and Li-ion transport within slurry-based composite cathodes. Reproduced with permission from Ref. [45] Copyright 2022, Elsevier. e) Diagram of a transparent $\text{Li}||\text{LPSC}||\text{LPSC-PTFE}||\text{LPSC}||\text{Cu}$ cell and a schematic highlighting Li dendrite interactions with PTFE in the LPSC-PTFE layer (inset), and f) time-lapse optical microscopy images recorded through the transparent side wall during Li plating at 2 mA cm^{-2} , the dashed orange, blue, red, and green lines delineate the Cu electrode, thin LPSC layer, LPSC-PTFE indicator layer, thick LPSC layer, and Li electrode, respectively, as shown in (e). Copyright 2024, Royal Society of Chemistry. Reproduced with permission from Ref. [48] Copyright 2024, Royal Society of Chemistry.

to 1.9 mS cm^{-1} and establishes uniform local current density on the Li surface (Figure 4b), effectively suppressing dendrite formation. Concurrently, WS_x facilitates FSI^- decomposition, forming Li_2S -rich inorganic components within the SEI. $\text{Li}||\text{Li}$ symmetric cells exhibit stable overpotentials of 63 mV at 0.1 mA cm^{-2} and cycle over 5500 h , while soft-pack SPAN||Li cells achieve an initial discharge capacity of 1048 mAh g^{-1} , highlighting the efficacy of sulfur-vacancy engineering in stabilizing ASSLIBs. Li et al. further

advanced electrolyte design by fabricating ultrathin flexible CSE membranes combining $\text{Li}_{10}\text{GeP}_2\text{S}_{12}$ with PVDF-HFP and a silane coupling agent to form organic–inorganic heterojunctions.^[52] Molecular dynamics (MD) and diffusion analyses indicate that the silane agent and $\text{Li}_{10}\text{GeP}_2\text{S}_{12}$ establish crosslinked networks and directional Li-ion pathways (Figure 4c), enhancing electrostatic and coordination interactions with TFSI^- . The resulting system achieves a room-temperature ionic conductivity of 0.105 mS cm^{-1} ,

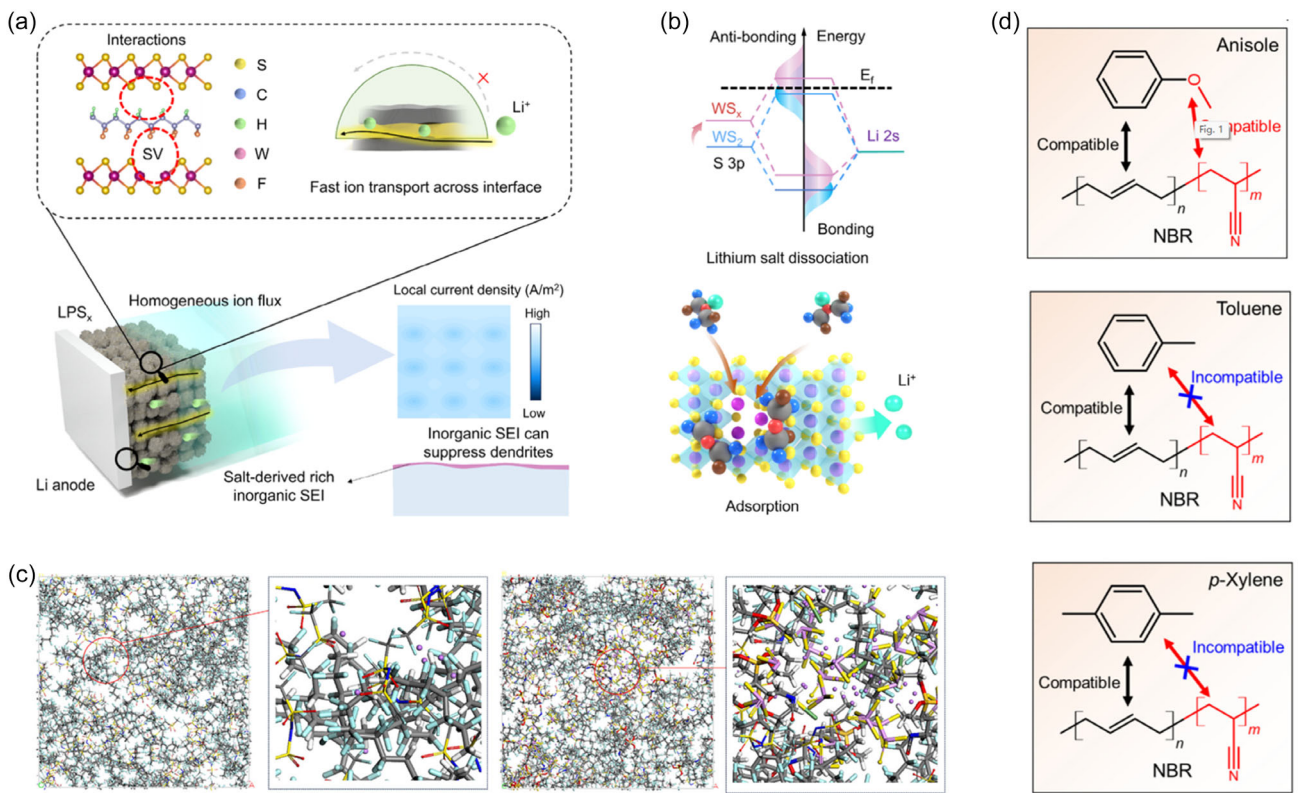


Figure 4. a) Diagram depicting Li-ions transport pathways and the interactions between PVDF-HFP and WS_x in the LPS_x composite polymer electrolyte (CPE). b) The influence of band engineering on p band elevation, s-p hybridization, and the corresponding LiFSI dissociation and absorption processes on the surface of WS_x. Reproduced with permission from Ref. [51] Copyright 2025, Wiley. c) Simulated structures of PVDF-HFP and PILS for obtain the diffusion time of Li-ion transport of PVDF-HFP and PILS. Reproduced with permission from Ref. [52] Copyright 2025, Wiley. d) Molecular compatibility between each unit of NBR polymer and solvents (anisole, toluene, and p-xylene). Reproduced with permission from Ref. [53] Copyright 2025, Elsevier.

an electrochemical stability window up to 4.9 V, and Li symmetric cell cycling stability over 3000 h. In ASSLSBs, the electrolyte supports a specific discharge capacity of 12 874 mAh g⁻¹ over 120 cycles, demonstrating that interfacial adhesion and controlled heterostructure design are crucial for optimizing Li-ion transport, maintaining space-charge regions, and ensuring high electrochemical performance.

ASSLIBs using SSE offer promising safety and energy-density advantages. NBR is widely used as a binder due to its moderate solubility in nonpolar solvents and chemical inertness toward SSEs. However, the polarity mismatch between butadiene and acrylonitrile units affects solvent compatibility and electrode performance. Choi et al. systematically studied the influence of solvent-NBR interactions, demonstrating that anisole effectively activates acrylonitrile units, promoting extended polymer conformations that establish strong adhesion with electrode materials and current collectors.^[53] In contrast, nonpolar solvents such as toluene or xylene induce polymer chain contraction, forming dense acrylonitrile cores with weakly interacting butadiene aggregates, reducing dissolution and interfacial contact (Figure 4d). Using anisole as the NBR solvent, graphite-silicon composite anodes exhibit enhanced mechanical robustness, allowing stable ASSLIB operation under low stack pressures of 16 MPa. This system delivers an initial capacity of 480 mAh g⁻¹, surpassing the

390 mAh g⁻¹ of NBR/toluene-based electrodes, while stress analysis confirms that acrylonitrile activation mitigates internal stress accumulation, effectively reinforcing electrode integrity and cycling stability.

The introduction of binders into SSE has become an important strategy for enhancing the overall performance of electrodes. Table 1 compares different binder systems with the corresponding sulfide electrolytes and their electrochemical performance, including ionic conductivity, cathode selection, cycling stability, and rate capability. It can be observed that the compatibility between binders and sulfide electrolytes has a significant impact on battery performance: certain binders can effectively improve interfacial contact while maintaining high ionic conductivity, thereby enhancing cycling life and rate capability. In contrast, poorly matched binders may increase interfacial resistance and thus limit electrochemical performance. However, some inconsistencies and limitations still exist in current studies. For example, the relationship between binder content and ionic transport behavior remains inconclusive across different reports; in some systems, the incorporation of binders improves mechanical stability but impedes ion migration or induces side reactions. In addition, certain polymeric binders exhibit chemical instability or risk interfacial reactions with sulfide electrolytes under long-term cycling or wide-temperature operating conditions, which restricts their practical applications.

Table 1. Electrochemical performance of different binder-based SSE systems.

SSEs	Ionic conductivity [mS cm ⁻¹ @°C]	Cathode	Performance [mAh g ⁻¹ @C@°C@Cycle number]	Rate [mAh g ⁻¹ @C]	Reference
Li ₆ PS ₅ Cl-Ionomer	0.016@RT	NCM712	142@0.5@25@300	123@2	[38]
Li ₆ PS ₅ Cl-Spandex	10@RT	—	—	—	[39]
LPSCL@PVDF-TrFE	1.2@RT	NCM811	83@1.61@RT@20000	189@0.16	[40]
PVdF-HFP	3.7@RT	LiNi _{0.70} Co _{0.15} Mn _{0.15} O ₂	146@0.5@30@200	160@0.2	[41]
GPE/LPS	3.6@60	Sulfur	700@1/20@60@130	—	[42]
Li ₆ PS ₅ Cl-NBR25	—	NCM712	150@0.2@RT@100	115@1	[43]
E-Li ₆ PS ₅ Cl	1.1@RT	NCM811@LPSCL	150@0.1@RT@150	98@1	[44]
Li ₆ PS ₅ Cl @PVdF-CTFE	10@60	NCM712	198.5@0.1@60@300	88@1	[45]
Li ₆ PS ₅ Cl-Li _x La ₃ Zr ₂ O ₁₂	0.303@RT	NCM424	163@0.1@70@50	—	[47]
LCO-Li ₆ PS ₅ Cl	—	PVDF-LCO	115@0.5@RT@200	60@2	[49]
Li ₆ PS ₅ Cl-Nafion-Li	1.53@RT	NCM711	148@0.5@RT@200	100@1	[50]
SVs-CPEs	1.9@RT	SPAN	1100@0.5@RT@500	—	[51]
Li ₁₀ GeP ₂ S ₁₂ -PVDF-HFP	0.11@RT	LiFePO ₄	150@0.5@RT@950	—	[52]
Li ₆ PS ₅ Cl-NBR	2.1@RT	—	—	—	[53]

Therefore, future research should focus on more systematic optimization of binder molecular design and interfacial reaction regulation. Overall, the rational selection and design of binders can not only optimize electrode structural stability and ion transport pathways but also provide a practical route toward achieving high-performance sulfide-based ASSLIBs.

2.2. Gel Polymers in SSEs

Since gel electrolytes, such as PEO, also exhibit excellent flexibility, incorporating gel electrolytes into sulfides can effectively address issues such as poor interfacial contact and electrolyte cracking in solid-state electrolytes.^[54,55] The soft polymer chains of gel polymers form a pliable buffer layer between sulfide particles and electrode materials, filling microcracks and voids, distributing mechanical stress, and establishing physical adsorption or weak chemical interactions via ether oxygen groups ($-\text{CH}_2-\text{CH}_2-\text{O}-$) with the sulfide surface or active materials, thereby enhancing wetting and reducing interfacial resistance.^[56] Simultaneously, gel polymers introduce a flexible phase into the brittle sulfide framework, lowering the overall elastic modulus of the composite electrolyte, maintaining structural integrity during volume changes, absorbing local stress, and suppressing crack propagation, which collectively improves cycling stability.^[57]

Building on this principle, Zou et al. designed an interfacial modification strategy by introducing a CPE (PEO/LiTFSI) between Li₆PS₅Cl and Li metal.^[58] The CPE provides high ionic conductivity and good interfacial compatibility while preventing direct Li-Li₆PS₅Cl contact. Symmetric Li||CPE/Li₆PS₅Cl/CPE||Li cells cycled stably at 60 °C and 0.2 mA cm⁻² for over 140 h, outperforming LiFePO₄||Li₆PS₅Cl||Li cells, which suffered rapid fading. Notably, LiFePO₄||Li₆PS₅Cl/CPE||Li cells achieved an initial capacity of 93.7 mAh g⁻¹ with 75.1% retention after 15 cycles at 0.5 C, demonstrating the promise of polymer-mediated interfacial designs for practical ASSLMBs. Kamikawa et al. further advanced interfacial

engineering by fabricating a LiF-rich protective layer using a Li₆PS₅Cl/(PFPE-ethoxydiol/LiTFSI) CPE.^[59] Density functional theory (DFT) simulations revealed that PFPE-ethoxydiol coordinates with Li and P atoms on the Li₆PS₅Cl surface, forming selective P—O bonds and stabilizing interfacial structures (Figure 5a). Experimentally, the composite displayed an ionic conductivity of 0.34 mS cm⁻¹ at 25 °C and enhanced reductive stability against Li metal compared with pristine Li₆PS₅Cl. The improvements arise from the in situ generation of a LiF-rich interphase, effectively acting as an artificial SEI. Additionally, LiTFSI decomposition products further reinforced interfacial stability. Symmetric Li||Li cells with this electrolyte demonstrated excellent cycling durability, confirming its potential as a robust interlayer for sulfide-based ASSLIBs.

Su et al. introduced an ASSLMBs using a flexible PEO-Li₁₀Si_{0.3}P_{1.7}S_{6.7}Cl_{1.8} (LSPSCl)-C-LiTFSI cathode (FCC) paired with a PEO-LSPSCl-LiTFSI CPE (S-CPE).^[60] Unlike traditional cathodes, sulfide electrolytes mixed with conductive additives can also undergo conversion reactions, suggesting their dual role as electrolytes and active materials. The FCC was fabricated similarly to the S-CPE by blending PEO, LSPSCl, and CNTs, yielding membranes with uniform LSPSCl dispersion in the polymer matrix. Figure 5b,c presents the photograph of S-CPE and the cross-section SEM image of Li||S-CPE||FCC cells. The results demonstrated that FCC exhibits excellent mechanical properties. It was also observed from the figure that the introduction of polymers has significantly improved the interface characteristics. Assembled Li||S-CPE||FCC cells cycled between 1.5–3.0 V exhibited redox activity linked to S/Li₂S conversion. Electrodes with lower CNT content suffered polarization and reduced capacity, while an optimized LSPSCl:_CNT ratio of 1:2 delivered an initial capacity of 414 mAh g⁻¹ at 0.1 A g⁻¹, retaining 97.8% after 100 cycles. Even at 0.4 A g⁻¹, cells retained 80% capacity after 500 cycles. Interfacial analyses revealed that Li/S-CPE contacts formed Li₂O, LiF, and Li₂S-rich layers, effectively suppressing dendrites, in contrast to Li/PEO interfaces dominated by resistive Li₂CO₃. In situ microscopy confirmed that cycling stability originated from

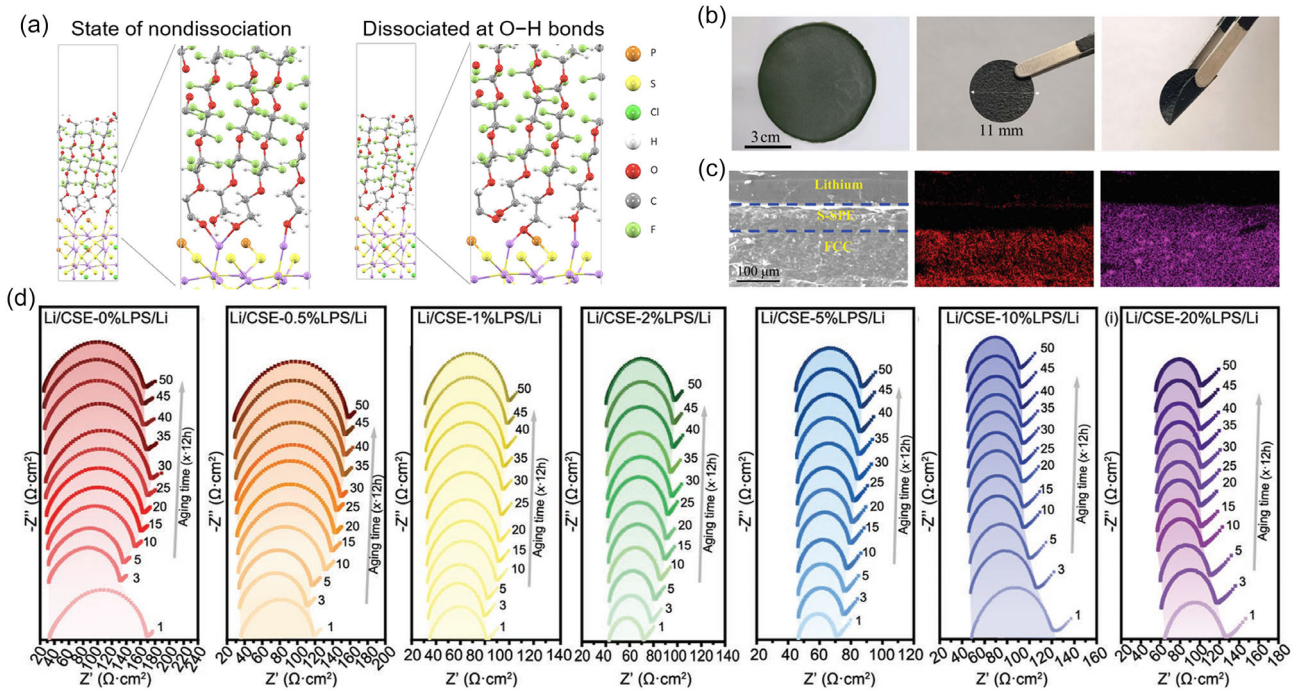


Figure 5. a) Simulated atomic structures of the PFPE-ethoxy-diol/Li₆PS₅Cl interface with four polymer chains in nondissociated and O–H bond–dissociated states. Reproduced with permission from Ref. [59] Copyright 2022, American Chemical Society. b) Photographs of the flexible composite cathode and c) cross-sectional SEM image of an ASSLIBs, accompanied by corresponding C and S elemental mapping. Reproduced with permission from Ref. [60] Copyright 2022, Wiley. d) Representative Nyquist plots of Li/CSE/Li cells incorporating CSE-x%LPS ($x = 0\text{--}20$ wt%) at 60 °C over 600 h, recorded in the frequency range 1 MHz–0.1 Hz. Reproduced with permission from Ref. [61] Copyright 2022, Wiley.

reversible P–S–P shuttling enabled by PEO segmental mobility. These results highlight FCC/S-CPE systems as promising designs for high-energy ASSLSBs with mitigated polysulfide shuttling and enhanced interfacial stability. Building on interfacial stabilization, Xu et al. developed a strategy to generate an LPS-containing SEI in situ at the Li/PEO-sulfide CSE interface.^[61] LPS, fully soluble in acetonitrile, was uniformly dispersed in the PEO matrix to tune SEI chemistry. Impedance spectra revealed that trace LPS ($\leq 0.5\%$) could not sustain interfacial stability, with resistance initially decreasing but subsequently rising due to instability, as shown in Figure 5d. By contrast, moderate LPS contents (1–5%) lowered the interfacial resistance to 12–24 Ω·cm² and maintained it over 600 h, while higher loadings (10–20%) stabilized resistance within 100–200 h. The in situ reaction of LPS with Li produced a LPS/Li₂S/LiF composite interphase, combining high ionic conductivity with dendrite suppression. Symmetric Li cells incorporating LPS-modified CSE exhibited long-term cycling stability exceeding 3475 h at 60 °C and 0.2 mA cm⁻², along with a critical current density of 0.9 mA cm⁻². Moreover, LiFePO₄||CSE||Li full cells retained 127.6 mAh g⁻¹ after 1000 cycles at 1 C, underscoring the durability of the engineered SEI layer.

Bilayer ASSLIBs integrating ceramic and polymer electrolytes offer improved performance over single-phase systems, yet interfacial resistance at heterogeneous junctions remains a critical limitation. Polizos et al. elucidate the structure–property relationships in SSE-polymer hybrid systems, demonstrating how the composite architecture and polymer chain dynamics synergistically govern Li-ion transport mechanisms.^[62] Using PEO matrices with LiTFSI

or LiFSI salts and Al-doped Li₇La₃Zr₂O₁₂ (Al-LLZO) nanosheets, they linked interfacial morphology and chemical interactions to conductivity. Dielectric relaxation spectroscopy distinguished strongly bound versus high-mobility Li-ion, showing that Al-LLZO increased the fraction of mobile ions. Small-angle X-ray scattering (SAXS) revealed nanoscale features (Figure 6a–d): PEO exhibited lamellar crystallinity with long periods of 30.2 nm at 25 °C and 36.0 nm at 60 °C, while PEO/LiFSI displayed scattering from salt clusters that partially dissociated at elevated temperatures. MD simulations confirmed that LiFSI forms small, labile aggregates that promote Li⁺ release into amorphous pathways, enhancing mobility. By contrast, LiTFSI clusters remained more stable, restricting ion dissociation and transport.

Ghorbanzade et al. used solid-state NMR to probe interfacial reactions in PEO-LiTFSI/Li₆PS₅Cl composite electrolytes, focusing on Li-ion exchange between organic and inorganic phases, a key factor governing macroscopic transport.^[63] Using ⁷Li–⁷Li and ⁶Li–⁶Li exchange spectroscopy (EXSY) (Figure 6e,f), they identified crosspeaks indicative of Li-ion migration between Li₆PS₅Cl and PEO matrices, while control experiments confirmed this process as genuine chemical transfer rather than spin diffusion. Despite these observations, bulk ionic conductivity remained nearly unchanged upon Li₆PS₅Cl incorporation, revealing that the exchange rate was too slow to create effective percolation pathways. The kinetics of interfacial exchange, dependent on interphase thickness and thermodynamic conditions, further constrained its practical contribution. In addition, interfacial reactions between LiCl/LPS in Li₆PS₅Cl and PEO

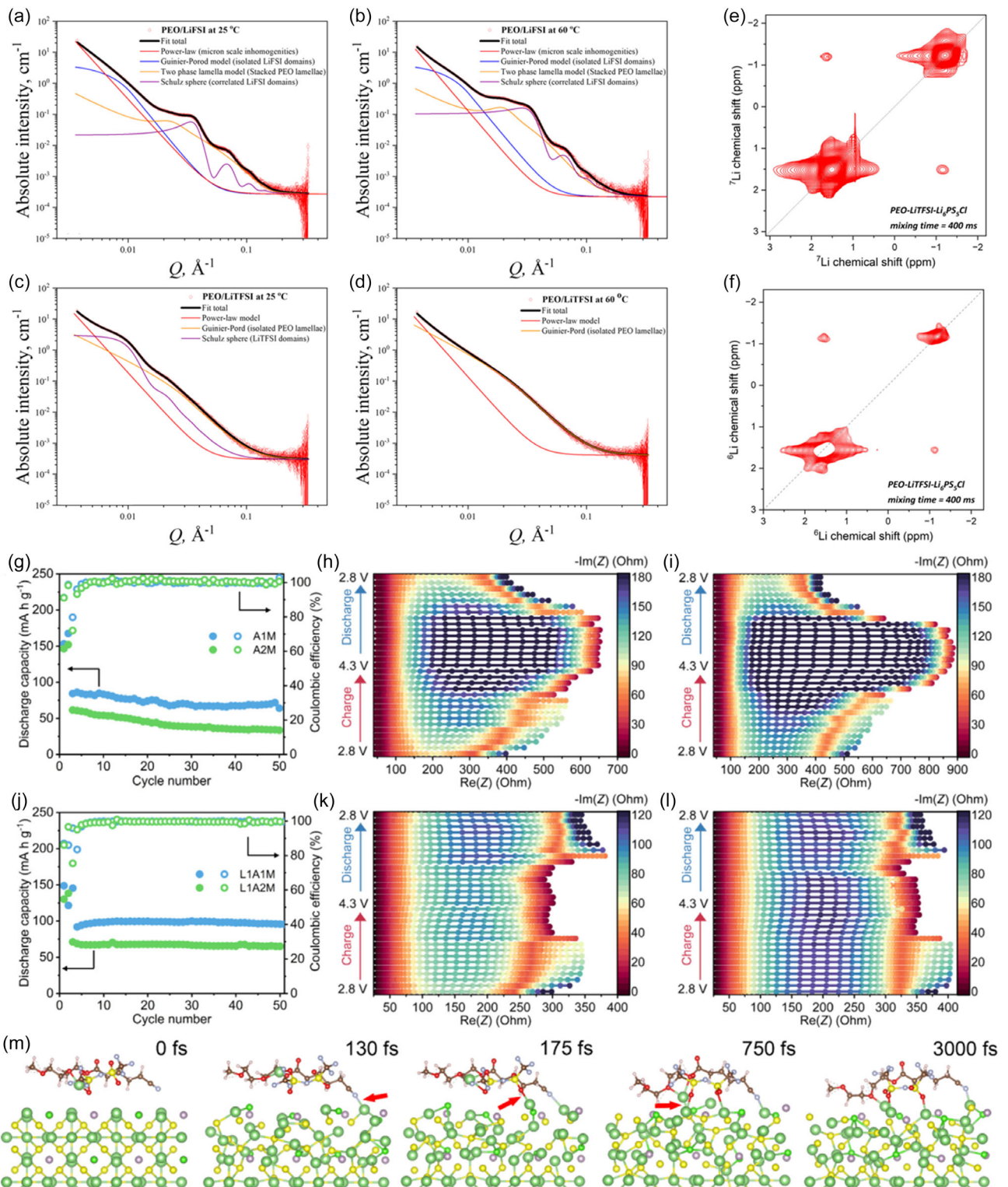


Figure 6. a,b) Experimental SAXS patterns and corresponding model fits of PEO/LiFSI electrolytes at 25 and 60 °C. c,d) PEO/LiTFSI electrolytes under identical conditions. Model fits were derived from multiple SAXS functions as indicated. Reproduced with permission from Ref. [62] Copyright 2024, American Chemical Society. e,f) ⁷Li-⁷Li and ⁶Li-⁶Li EXSY NMR spectra of PEO-LiTFSI-Li₆PS₅Cl at a 400 ms mixing time, showing off-diagonal correlations characteristic of spontaneous and reversible Li-ion exchange between PEO-LiTFSI and Li₆PS₅Cl phases. Reproduced with permission from Ref. [63] Copyright 2024, Wiley. g) Cycling performance of NCM||Li cells at 0.5 C and corresponding in situ impedance spectra of h,i) NCM||A1M||Li and j-l) NCM/L1A1M||Li cells during the first and second cycles. m) AIMD simulation of the copolymer/LPSC interface, revealing Li⁺ exchange pathways. Reproduced with permission from Ref. [64] Copyright 2024, Elsevier.

generated complexes with restricted mobility, further suppressing Li^+ transport. Although bromine doping enhances $\text{Li}_6\text{PS}_5\text{Cl}$ conductivity by inducing structural disorder and Li vacancies, it simultaneously intensifies interfacial side reactions. Overall, while EXSY confirmed spontaneous Li-ion exchange across polymer-sulfide interfaces, its sluggish dynamics and chemical by-products critically limit ionic conduction. These findings underscore the importance of interfacial design and kinetic control for optimizing composite solid electrolytes in next-generation ASSLIBs. In a complementary approach, Yuan et al. developed a high-voltage-stable ether-nitrile copolymer electrolyte via in situ polymerization and examined the synergistic effects of argyrodite sulfides and nano- Al_2O_3 on performance.^[64] PEO-based electrolytes suffered severe capacity fade, while a copolymer (A1M) improved retention to 83.5% after 50 cycles at 0.5 C, compared with 72.3% for P(PEGMA). The improvement arose from higher ionic conductivity and more stable SEI/CEI formation. In situ impedance measurements showed A1M experienced a sharp resistance rise to $\approx 600\ \Omega$ at 4.3 V, whereas sulfide-containing systems (L1A1M, L1A2M) stabilized quickly after initial SEI formation, maintaining low interfacial impedance. Even modest sulfide addition (1%) slightly enhanced conductivity (A1M: $0.0792\ \text{mS cm}^{-1}$; L1A1M: $0.104\ \text{mS cm}^{-1}$), but the major benefit was interfacial stabilization rather than bulk conduction (Figure 6h–m). Ab initio MD (AIMD) simulations revealed rapid Li-ion migration from polymer to sulfide surfaces within femtoseconds (Figure 6n), accompanied by Li-S bond formation and dynamic coordination with nitrile and ether groups. Raman spectra confirmed enhanced Li-ion interaction with ether groups and partial dissociation from sulfonyl moieties upon sulfide addition. These results demonstrate that controlled polymer-sulfide interactions accelerate Li-ion exchange and improve stability, while excessive sulfide disrupts balance, offering mechanistic guidelines for designing high-performance polymer-inorganic composite electrolytes.

Zheng et al. introduced a sulfide composite electrolyte by combining PEO with air-stable Li_4SnS_4 , achieving a balance of chemical and electrochemical stability.^[65] The presence of Li_4SnS_4 facilitated Li-ion transport, leading to an ionic conductivity of $2.55 \times 10^{-2}\ \text{mS cm}^{-1}$. Building on this, Yuan et al. sought to resolve the intrinsic incompatibility between inorganic and organic phases.^[66] By chemically linking $\text{Li}_6\text{PS}_5\text{Cl}$ and PEO through (3-chloropropyl)trimethoxysilane (CTMS) on a 3D PET scaffold, they fabricated a CPE with remarkable properties, including high ionic conductivity ($0.75\ \text{mS cm}^{-1}$), wide electrochemical stability (up to 5.3 V vs. Li/Li^+), and strong mechanical robustness (9.35 MPa). This system enabled stable Li plating/stripping for 400 h at $0.3\ \text{mA cm}^{-2}$ with low polarization, while LiFePO_4 cells retained $163.6\ \text{mAh g}^{-1}$ over 100 cycles with nearly 100% CE. Beyond chemical bridging, interfacial engineering has also been explored to suppress dendrite growth and minimize resistance at the Li/sulfide interface. Incorporation of a lithium aluminum titanium phosphate (LATP)-PEO interlayer between $\text{Li}_{5.5}\text{PS}_{4.5}\text{Cl}_{1.5}$ and Li provided uniform filler dispersion, improved mechanical integrity, and significantly reduced side reactions. As a result, symmetric Li cells cycled stably for 2800 h at $0.2\ \text{mA cm}^{-2}$ and 60 °C with low interfacial resistance.^[67] In parallel, Thorat et al. developed a PEO/ $\text{Li}_{5.6}\text{PS}_{4.6}\text{Cl}_{1.4}$

composite electrolyte exhibiting high ionic conductivity ($0.126\ \text{m}\Omega^{-1}\ \text{cm}^{-1}$ at 40 °C).^[68] This design not only supported high Pyrene-4,5,9,10-tetraone (PTO) cathode loading (45 wt%) but also delivered a high specific capacity of $342.3\ \text{mAh g}^{-1}$ at 0.3 C, corresponding to 83.6% utilization. Excellent cycling stability was achieved over 500 cycles with >93% capacity retention and >98% CE.

In contrast to strategies relying on PEO, Mirmira et al. revealed its incompatibility in certain hybrid systems, where reactivity with LPS creates parasitic pathways that suppress overall conductivity. Substituting PEO with chemically inert polyethylene (PE) circumvented this issue, confining Li-ion transport to the inorganic phase and thereby improving ionic conductivity and cycling stability at 60 °C.^[69] Extending interfacial engineering to cathodes, Liang et al. proposed a “polymer-patched inorganic” coating, combining nanoscale LATP with cyclized PAN (cPAN) on single-crystal NCM622, as shown in Figure 7a,b.^[70] While LATP provided fast Li-ion transport and oxidative stability, cPAN repaired interfacial defects, resulting in a dense, conductive layer that enabled long-term stability, with a 72.7% capacity retention after 500 cycles at 0.5 C and high-rate performance of $87.3\ \text{mAh g}^{-1}$ at 2 C, significantly outperforming pristine cathodes. Zhu et al. reported a significant advance in ASSLIBs by integrating a selenium- and sulfur-rich polyacrylonitrile cathode (Se/S-S@pPAN) with a PEO-LLZTO electrolyte.^[71] A ball-milling strategy was used to restructure a sulfur-EVA electrode into a robust fibrous network, creating a stable 3D framework that uniformly encapsulated active species and electrolyte. This design facilitated nanoscale sulfur dispersion ($\approx 50\ \text{nm}$), while selenium incorporation enhanced redox kinetics through Se–S bond formation (Figure 7c,d). The resulting composite achieved high sulfur loading (60.9 wt%) and delivered excellent electrochemical performance, with discharge capacities of 1042 and $445\ \text{mAh g}^{-1}$ at 0.1 and 1 C, respectively. When paired with LiFePO_4 , the PEO-LLZTO electrolyte further enabled long-term cycling stability with $158.9\ \text{mAh g}^{-1}$ at 1 C and maintains 80% retention after 1000 cycles. Density functional theory calculations confirmed strong Li-O interactions between the PEO matrix and $\text{Li}_2\text{S}_n/\text{Li}_2\text{Se}_n$ species, revealing that spontaneous adsorption suppressed polysulfide dissolution and the shuttle effect. Building on this, the Zhu et al. also proposed a stress-buffering strategy by embedding a crosslinked EVA network within the sulfur cathode.^[72] The elastic framework accommodated volume expansion, reduced stress fluctuations by $\approx 33.7\%$, and maintained stable ion/electron pathways. As a result, S-EVA cathodes achieved a high areal capacity of nearly $3.0\ \text{mAh cm}^{-2}$ at $7.5\ \text{mg cm}^{-2}$ loading with excellent cycling stability. In situ pressure monitoring of all-solid-state lithium-sulfur batteries (ASSLSBs) (S-Pristine, S-PVDF, and S-EVA) further verified this effect: while all systems showed pressure increases during discharge, the S-EVA/LTO cells exhibited the smallest variation ($\approx 0.63\ \text{MPa}$) and the most gradual release upon charging (Figure 7e–g). This confirmed that the cross linked structure effectively mitigates mechanical stress and prolongs cycling stability.

Luo et al. investigated the chemical degradation of $\text{Li}_6\text{PS}_5\text{Cl}$ when combined with PEG, revealing that the high polarity of PEG perturbs the electronic structure and bonding of PS_4^{3-} tetrahedra, triggering side reactions.^[73] Interestingly, the terminal

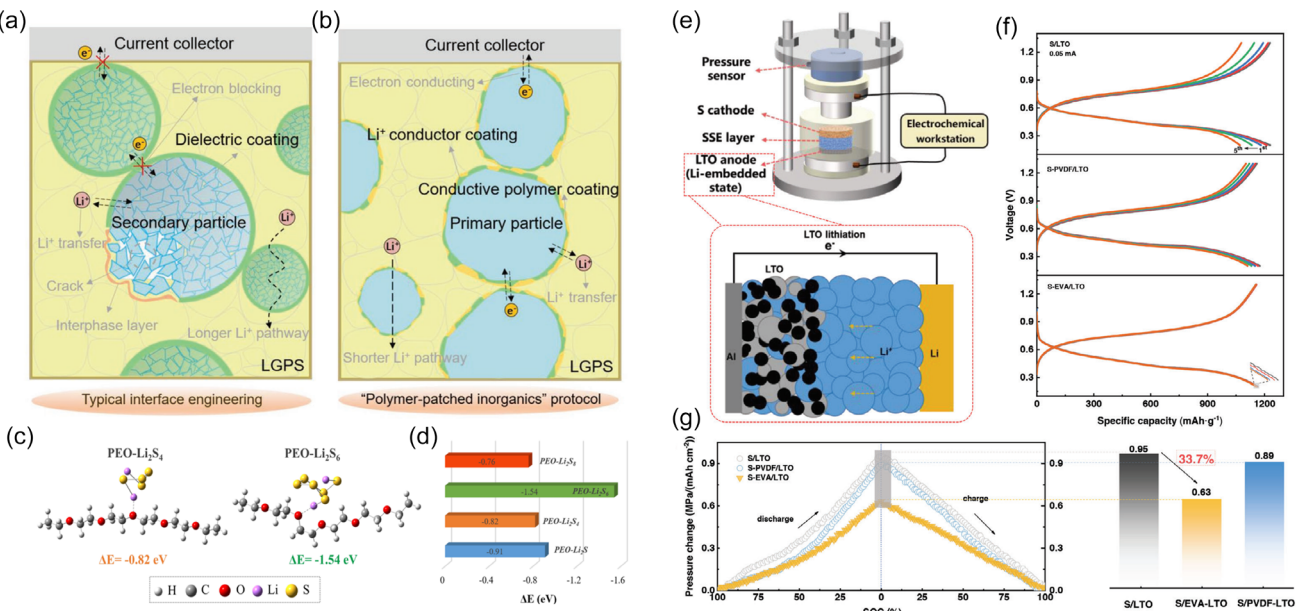


Figure 7. a) Schematic of conventional interface engineering and b) the "polymer-patched inorganic" coating strategy demonstrating improved interfacial stability. Reproduced with permission from Ref. [70] Copyright 2022, Wiley. c) Optimized adsorption configurations of various Li polysulfides on PEO chains and d) corresponding adsorption energies. e) Schematic of in situ pressure monitoring in all-solid-state cells using zero-strain LTO electrodes as counter electrodes. Reproduced with permission from Ref. [71] Copyright 2024, American Chemical Society. f) Discharge/charge voltage profiles of S/LTO, S/PVDF/LTO, and S-EVA/LTO cells at 50 °C. g) First-cycle pressure evolution of the three systems. Reproduced with permission from Ref. [72] Copyright 2024, Wiley.

groups of PEG not only stabilize the internal interface but also expand the electrochemical window of the composite electrolyte. Moreover, the in situ formation of a LiF-rich layer effectively suppresses unwanted reactions at the Li/electrolyte interface. Using in situ X-ray photoelectron spectroscopy (XPS), they monitored the evolution of the SEI on PEGDMEL@mix during Li deposition (Figure 8a–d). Waterfall plots of F 1s, S 2p, and O 1s signals revealed that early Li deposition ($t < 10$ min) induced LiFSI decomposition, forming LiF and Li_xS_yO_z species, alongside polysulfides from oxidative coupling of PS₄³⁻ tetrahedra. Subsequent reactions further converted Li₂S₂O₄ and polysulfides into Li₂S and Li₂O, which became the dominant SEI components after $t > 15$ min. This study elucidates the chemical evolution of polymer/sulfide composites and provides guidance for designing dendrite-suppressing interfacial layers. Separately, Zhang et al. tackled the shuttle effect in Li-sulfur systems by using sulfurized PAN (SPAN) as a solid-state cathode coupled with a GPE based on polyethylene glycol diacrylate (PEGDA).^[74] The quasisolid-state Li-SPAN batteries were fabricated via in situ thermal polymerization, forming a robust electrode-electrolyte interface with minimal damage to battery components. The PEGDA GPE exhibited high ionic conductivity (6.87 mS cm⁻¹ at 30 °C) and a wide electrochemical window of 4.53 V. The Li-SPAN cells achieved a specific capacity of 1217.3 mAh g⁻¹ after 250 cycles at 0.2 C, with 89.9% capacity retention, demonstrating that the synergistic combination of SPAN cathode and thermally polymerized PEGDA GPE provides a promising strategy for high-energy, safe ASSLSBs.

Yuan et al. developed a hybrid polymer blend of poly(1,3-dioxolane) and poly(polyethylene glycol diacrylate) via in situ polymerization, achieving robust electrochemical performance

in LiFePO₄||Li cells with an average CE above 99% at 0.5 C.^[75] Symmetric cells demonstrated stable cycling for over 1000 h. Computational analysis and compositional studies confirmed the stability of the polymer components, with Li salt decomposition forming a LiF-stabilized anode interface. On the cathode side, Li₃PO₄-coated NCM622 suppressed particle collapse and electrolyte decomposition, yielding 90.48% capacity retention after 200 cycles at 0.5 C at room temperature. In situ impedance and compositional analyses further validated interfacial stabilization strategies, highlighting an integrated approach to designing high-performance ASSLSBs. Similarly, Ma et al. coated a N-CNT network with polypyrrole (PPy) to enhance conductivity and compatibility with sulfide electrolytes (Figure 8e).^[76] The PPy@N-CNT network provided continuous electron pathways while mitigating local stress, as confirmed by in situ pressure measurements and AFM. This design reduced axial pressure by 11% at 30 °C with 3 mg cm⁻² sulfur loading. High-mass-loading cathodes (4.5 mg cm⁻²) achieved 6 mAh cm⁻² at 0.1 C (1348 mAh g⁻¹) with stable cycling over 300 cycles at 0.2 C, and even at 60 °C, delivered >8.8 mAh cm⁻², demonstrating the effectiveness of integrating flexible, conductive networks in solid-state conversion cathodes. Wang et al. reported a dual ion-electron conductive binder incorporating in situ reduced silver nanoparticles within an ether-rich polymer, enabling scalable, air-stable silicon anodes without relying on sensitive sulfide electrolytes (Figure 8f–g).^[77] The silicon anode achieved 1906.9 mAh g⁻¹ at 2 C (4.4 mA cm⁻²) under 5 MPa stack pressure, with stable cycling over 500 cycles. A full cell with an NCM90 cathode maintained excellent stability for 2000 cycles at 5 C (8 mA cm⁻²). This approach demonstrates a practical and low-cost strategy for

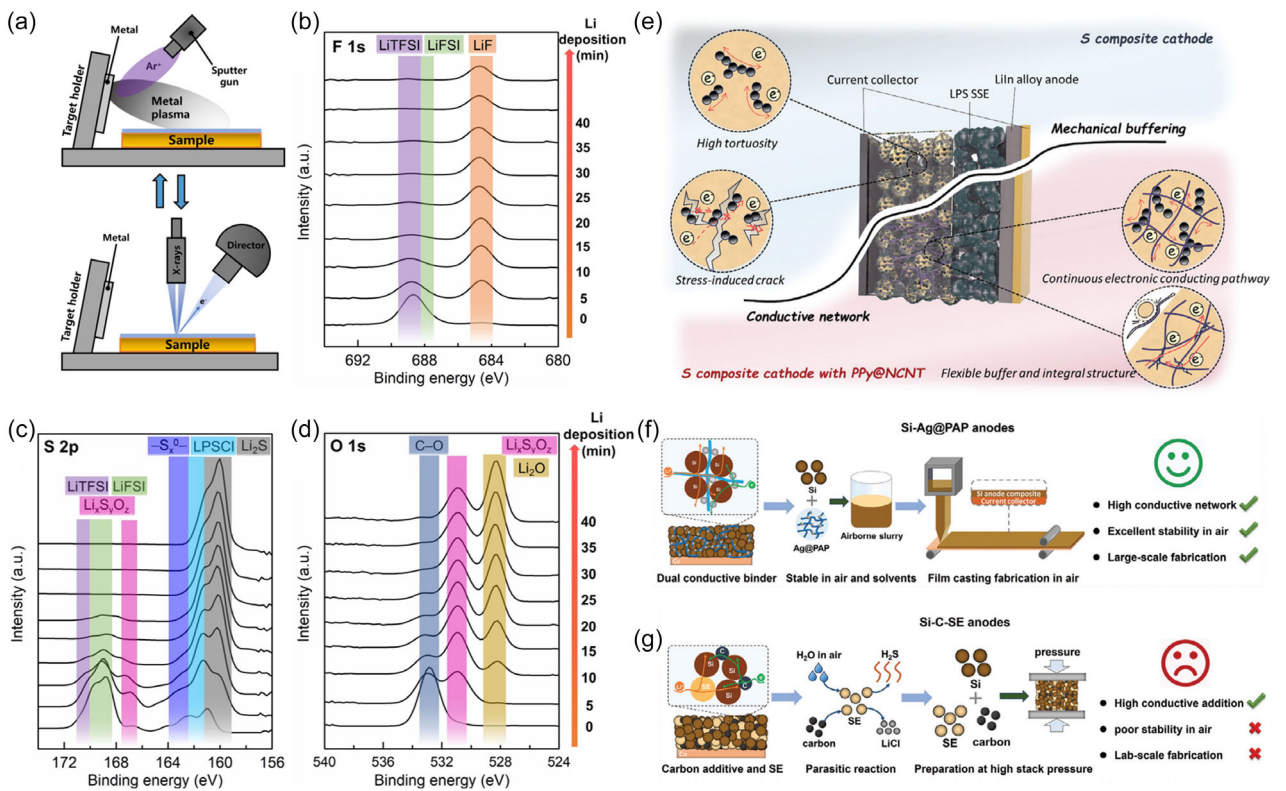


Figure 8. a) Schematic of the in situ XPS measurement during Li deposition. In situ XPS spectra showing the evolution of b) F 1s, c) S 2p, and d) O 1s signals at different Li deposition times. Reproduced with permission from Ref. [73] Copyright 2024, Wiley. e) Illustration of the continuous, flexible conductive network and its benefits for ASSLIBs. Reproduced with permission from Ref. [76] Copyright 2024, Wiley. f) Structure of Si-Ag@PAP anodes and g) Si-SE-C anodes, highlighting differences in conductivity, environmental stability, and manufacturability. Reproduced with permission from Ref. [77] Copyright 2024, Wiley.

fabricating high-performance all-solid-state silicon anodes with dual ion-electron conductivity.

Vuong et al. explored the role of self-polymerized dopamine-coated vapor-grown carbon fibers (PDA@VGCF) in enhancing ion-electron percolation within composite cathodes.^[78] They systematically evaluated electrochemical performance, charge transfer kinetics, and interfacial side reactions in cathodes composed of LiNi_{0.8}Co_{0.15}Al_{0.05}O₂, Li₆PS₅Cl, and VGCF. The PDA@VGCF-modified cathode achieved a higher discharge capacity of 165.5 mAh g⁻¹ at 0.1 C compared to 118.7 mAh g⁻¹ for bare VGCF, while maintaining ≥96% capacity retention over 100 cycles. This improvement was attributed to the PDA layer, which promoted Li-ion diffusivity, optimized cathode component distribution, and suppressed side reactions, highlighting surface modification of conductive additives as a promising strategy for sulfide-based ASSLIBs. Gu et al. investigated the temperature-dependent electrochemical behavior of ASSLIBs, explaining the differences in discharge curves at room temperature versus 60 °C by slow kinetics at lower temperatures.^[79] Using dP/dV analysis combined with spectroscopic studies, they revealed asymmetric sulfur redox pathways and species evolution during cycling. Ex situ Raman spectroscopy tracked the sulfur cathode at different states of charge, as shown in Figure 9a,b. For the 60 °C system, characteristic S₈ peaks (152.1, 218.7 and 474.6 cm⁻¹) were observed, while acetylene black displayed broad D- and G-bands. Notably, polysulfide intermediates

(Li₂S₄) and Li₂S peaks were absent throughout cycling, suggesting direct conversion mechanisms. At room temperature, S₈ peaks gradually disappeared during discharge, replaced by a broad feature, which then reversed upon charging. The absence of Li₂S₄ peaks at both temperatures aligns with previous reports, indicating consistent reaction pathways in ASSLIBs despite temperature variations.

Kim et al. investigated a ASSLIBs architecture comprising a Li₆PS₅Cl sulfide electrolyte layer between a composite cathode and a Li/In anode, encapsulated within an insulating mold and subjected to uniaxial pressure up to 300 MPa.^[20] Figure 9c presents the schematic of the evolution of side reactions and voids in Li₆PS₅Cl and the mitigation achieved by incorporating an ion-conductive polymer (ICP). The cathode included LiNi_{0.95}Co_{0.04}Al_{0.01}O₂, carbon nanofibers (\approx 100 nm \times 20–200 μ m), and Li₆PS₅Cl. Two major challenges were identified: interfacial side reactions and voids at solid–solid contacts, which hinder Li-ion transport. Incorporating an ICP into the cathode mitigated these issues by suppressing side reactions, filling voids, and establishing additional Li-ion pathways, while providing mechanical compliance during volumetric changes. The chemical and electrochemical compatibility of Li₆PS₅Cl with ICP solvents was systematically evaluated, identifying diethyl carbonate and anisole as stable candidates. Characterizations via EIS, XPS, and SEM confirmed a stable polymer–sulfide interface, enabling stable cycling over 100 cycles. Building upon interface engineering,

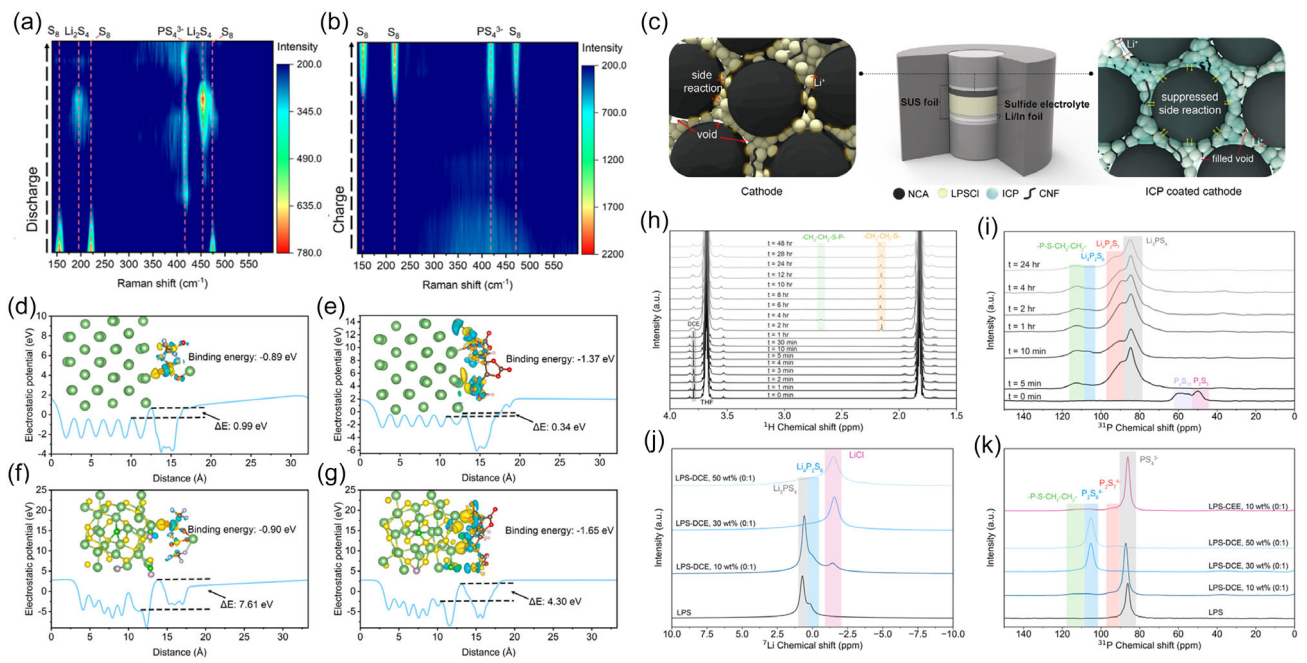


Figure 9. a,b) Waterfall plots and corresponding intensity maps of Raman spectra for the sulfur cathode in the SCC442/Li cell at different voltages during discharge (a) and charge (b) at 60 °C. Reproduced with permission from Ref. [79] Copyright 2024, American Chemical Society. c) Schematic illustrating the evolution of side reactions and voids in Li₆PS₅Cl and the mitigation achieved by incorporating an ICP. Reproduced with permission from Ref. [20] Copyright 2024, Wiley. d–g) Charge density difference and electrostatic potential distributions for Li (100)-LITFSI (d), Li (100)-PVCA (e), LPSC (100)-LITFSI (f), and LPSC (100)-PVCA (g). Reproduced with permission from Ref. [80] Copyright 2024, Elsevier. h–k) Evolution of crosslinking in the 10 wt% (0:1) reaction system: (h) ¹H NMR liquid-state NMR spectra at different times, (i) ³¹P and (j) ⁷Li solid-state NMR for varying DCE concentrations, and (k) ³¹P solid-state NMR of hybrids with increasing DCE and a 10 wt% CEE-derived hybrid. THF = tetrahydrofuran. Reproduced with permission from Ref. [34] Copyright 2024, American Chemical Society.

Mirmira et al. further highlighted the influence of polymer processing and morphology on hybrid sulfide electrolytes.^[31] They showed that solution casting of LPS with PE could alter LPS crystallinity, reducing ionic conductivity, whereas solvent-free ball milling achieved more uniform polymer distribution and higher conductivity, emphasizing the critical role of polymer–sulfide structure on electrochemical stability. Complementing these approaches, Yuan et al. prepared PEC-coated sulfide composite electrolytes via wet ball milling and in situ polymerization.^[80] These ultraflexible particles formed dense, binder-free structures under cold pressing, while a LiF-rich interface on the Li anode enhanced stability. The critical current density increased to 2.0 mA cm⁻², enabling symmetric Li cells to cycle stably at 0.5 mA cm⁻² for 2000 h. NMC622||Li cells maintained high initial capacities (173.5 mAh g⁻¹) over 300 cycles without short circuits. Electrostatic potential analysis showed the polymer–sulfide interface effectively suppressed electron migration, with a potential barrier exceeding 4 eV (Figure 9d–g). Wang et al. introduced a flame-retardant, self-healing polyurethane-thiourea polymer grafted onto Li₂P₂S₁₁ (SHPUSB-40%LPS), achieving high ionic conductivity (\approx 1 mS cm⁻¹), elastic modulus at MPa level, and compatibility with silicon anodes.^[57] FSI⁻ anions strongly adsorbed onto sulfur vacancies, enhancing Li-ion transport and reducing activation energy by 40%. Dynamic disulfide and hydrogen bonds enabled adaptive self-assembly at the interface, mitigating volume-change stress. A Si anode retained 53.5% capacity after 300 cycles, and a 2 Ah-scale Si||NMC622 pouch cell maintained 76.3% capacity over 350 cycles at 0.5 C, demonstrating the potential

of self-healing solid electrolytes for scalable, high-performance applications.

Mirmira et al. introduced a transformative one-pot *in situ* synthesis strategy to generate SCE with tunable chemical and structural properties.^[34] To elucidate the reaction mechanism, they systematically tracked intermediate species in both the liquid supernatant and solid precipitate during the reaction of a Li₂S/P₂S₅-DCE system (10 wt%, 0:1 ratio). ¹H NMR spectra (Figure 9h) of the THF supernatant revealed complete consumption of DCE monomers within 2 h, accompanied by the emergence of peaks at 2.1 and 2.65 ppm. Comparison with solution-state ¹H NMR of the reference molecule TTP identified the 2.65 ppm peak as the covalent linkage between LPS and organic groups, while the 2.1 ppm signal corresponded to thioether units ($-\text{CH}_2-\text{CH}_2-\text{S}-$) from nonbonded oligomers formed between Li₂S and DCE. The crosslinking degree, determined from peak area ratios, steadily increased over 2–6 h, stabilizing at 12%. Solid-state ³¹P NMR provided direct evidence of covalent bond formation (Figure 9i). Samples dried at 80 °C to preserve intermediates showed that P₂S₅ converted fully to LPS within five minutes, with crosslinking signals absent in the liquid phase due to low concentrations of early products. Peak deconvolution revealed increasing integrals of $-\text{P}-\text{S}-\text{CH}_2-\text{CH}_2-$ groups consistent with the 12% crosslinking observed in ¹H NMR, confirming that complete LPS formation is a prerequisite for covalent crosslinking in the Li₂S/P₂S₅/DCE system. Increasing DCE content (30–50 wt%) led to incomplete reactions, evidenced by ⁷Li NMR (Figure 9j) detection of LiCl and unreacted

Li_2S , and ^{31}P NMR (Figure 9k) peaks corresponding to $\text{Li}_4\text{P}_2\text{S}_6$, indicating that covalent bonding cannot occur without full LPS formation. The *in situ* strategy proved broadly generalizable. Using alternative monomers such as 2-chloroethoxyethane (CEE) or 1,4-dichlorobutane (DCB), ^{31}P NMR confirmed covalent crosslink formation, while ^7Li NMR and solid-state ^1H NMR verified full $\text{Li}_2\text{S}/\text{P}_2\text{S}_5$ conversion and polymer incorporation. This versatility allows systematic tuning of halogen type (Cl, Br, etc.), organic moieties (ether chains, alkanes), and connectivity functionality (di- or tri-halogen) according to application needs. Using DCE as a model, synchronous formation of inorganic and polymer phases produced a microstructure with uniform inorganic–polymer distribution and covalent bonds at specific ratios. When incorporated into Li metal batteries, the hybrid electrolytes exhibited enhanced mechanical integrity, improved ionic conductivity, and superior cycling stability compared with conventional ex situ “polymer + sulfide” blends. These findings establish a new paradigm for designing inorganic–polymer electrolytes, demonstrating a wide chemical space for hybrid materials with potential for diverse applications.

Wang et al. explored the compatibility of the $\text{Li}_{10}\text{GeP}_2\text{S}_{12}$ (LGPS) sulfide electrolyte with eight nonprotic solvents to define an optimal polarity range.^[81] To assess the impact of oxygen and moisture under practical manufacturing conditions, they exposed selected solvents to dry air, nitrogen, or water-containing vapor, highlighting their detrimental effects. Ultimately, dimethyl carbonate (DMC) and the PVDF-HFP were chosen to prepare $\text{Li}_{10}\text{GeP}_2\text{S}_{12}$ -based composite electrolytes ($\approx 40 \mu\text{m}$ thick) with an ionic conductivity of 2 mS cm^{-1} . The process involved homogenizing $\text{Li}_{10}\text{GeP}_2\text{S}_{12}$ powders (1–5 μm , SEM in Figure 10a) with PVDF-HFP in DMC, followed by coating and solvent evaporation. DMC was selected for its minimal effect on $\text{Li}_{10}\text{GeP}_2\text{S}_{12}$ conductivity and its status as a green solvent. By varying polymer content, a series of $\text{Li}_{10}\text{GeP}_2\text{S}_{12}$ membranes with thickness comparable to commercial separators were obtained. Top-view images of LPCE-5 (Figure 10a) reveal uniform microstructure and self-supporting morphology, with visible polymer fibers indicating effective particle binding. Assembly involved stacking Li/G electrodes with the LPCE membrane, followed by 200 MPa molding and continuous 100 MPa compression during testing

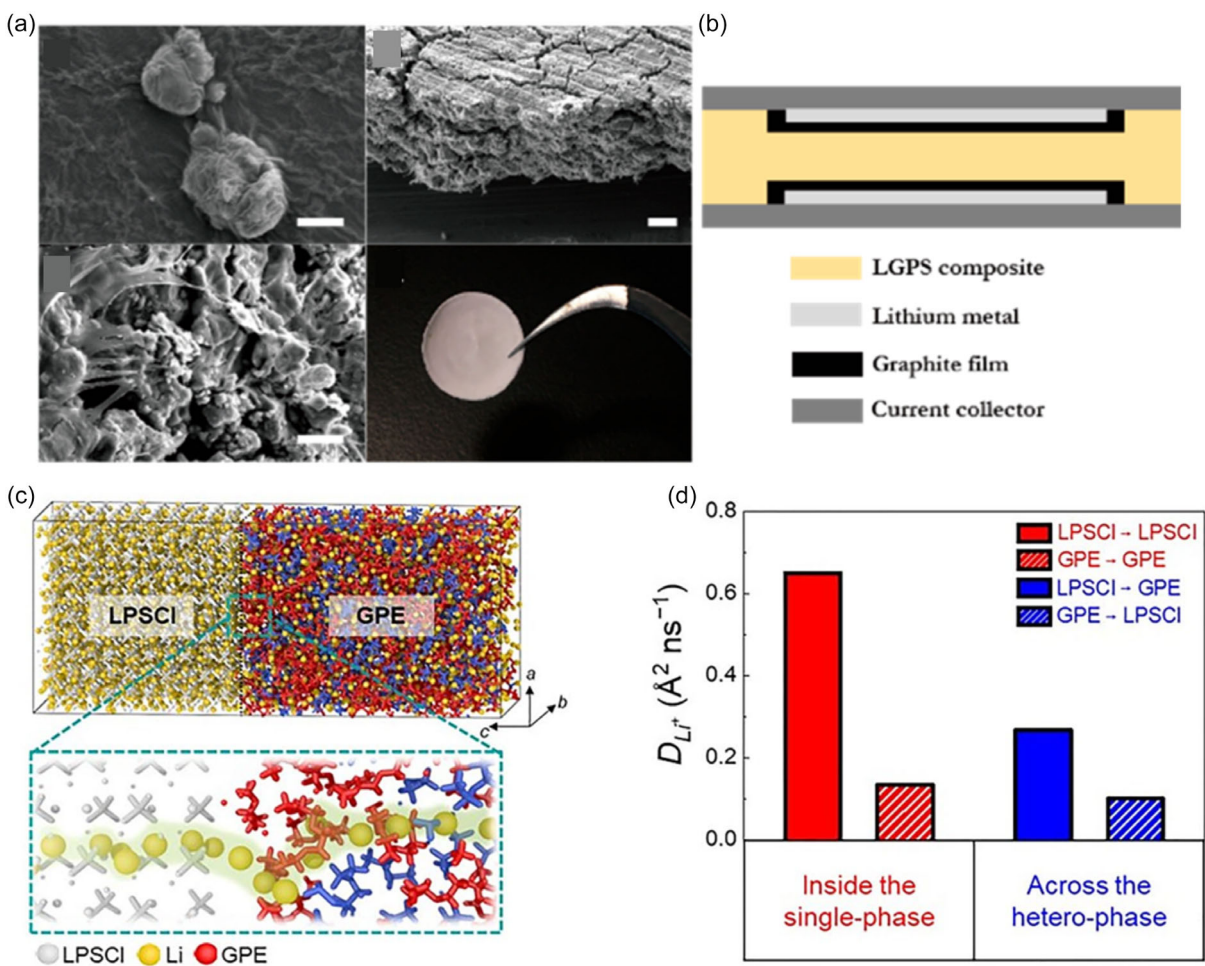


Figure 10. a) SEM images of pristine LGPS particles (scale bar = 2 μm), cross-sectional and top views of LPCE-5 (scale bars = 10 μm), and optical image of the self-supporting LPCE-5 membrane. b) Schematic of Li/G+LPCE cell assembly. Reproduced with permission from Ref. [81] Copyright 2024, American Chemical Society. c) Model systems representing Li-ion conduction across the $\text{Li}_6\text{PS}_5\text{Cl}$ -GPE hetero-phase interface in CSEs. d) D_{Li^+} in single-phase $\text{Li}_6\text{PS}_5\text{Cl}$ and GPE, and across the hetero-phase interface. Reproduced with permission from Ref. [82] Copyright 2024, Springer Nature.

(Figure 10b). A graphite protective layer was applied to mitigate direct Li-Li₁₀GeP₂S₁₂ contact, enhancing interfacial stability. Nyquist analysis of LPCE symmetric cells shows a mid-to-high frequency semicircle corresponding to interfacial impedance and a low-frequency Warburg tail. Increasing polymer content from 5 to 20 wt% raised both bulk and interfacial impedance, reflecting improved film formation but reduced ionic conductivity, particularly at the interface. LPCE-5 emerged as the optimal composition, combining processability with an ionic conductivity of ≈ 2 mS cm⁻¹ and area conductivity of ≈ 500 mS cm⁻². It sustained over 450 h of cycling at 0.5 mA cm⁻², maintaining 0.5 mAh cm⁻² surface capacity while tolerating tenfold current pulses. Building on ion transport understanding, Oh et al. constructed a mechanistic model for CSEs, focusing on dual-continuous Li-ion channels and interfacial conduction across inorganic-polymer boundaries.^[82] MD simulations compared Li⁺ mobility in pure Li₆PS₅Cl, pure GPE, and heterogeneous Li₆PS₅Cl-GPE interfaces (Figure 10c). Mean squared displacement (MSD) and diffusion coefficients (D_{Li^+}) revealed that Li-ion mobility was substantially lower at the heterogeneous interface: pure Li₆PS₅Cl ($0.65 \text{ \AA}^2 \text{ ns}^{-1}$) $>$ Li₆PS₅Cl region within the interface ($0.27 \text{ \AA}^2 \text{ ns}^{-1}$) $>$ pure GPE ($0.13 \text{ \AA}^2 \text{ ns}^{-1}$) $>$ GPE region in the interface ($0.10 \text{ \AA}^2 \text{ ns}^{-1}$), emphasizing the interfacial barrier effect. The CSE consisted of argyrodite-type Li₆PS₅Cl embedded in a GPE where Li⁺-glyme complexes mediate conduction. Ionic

percolation in Li₆PS₅Cl strongly depended on GPE elasticity, and controlled solvation/desolvation of Li⁺-glyme complexes enhanced interfacial transport. Scalable CSE membranes ($8 \times 6 \text{ cm}$, $\approx 40 \mu\text{m}$) were combined with high-loading NCM711 cathodes (39 mg cm^{-2}) and graphite anodes (N/P = 1.1) into bipolar all-solid-state cells, achieving a volumetric energy density up to 480 Wh L^{-1} at 25°C with excellent cycling stability, surpassing previously reported CSE-based systems.

The inherent viscosity of solid electrolytes offers a significant advantage for ASSLIBs assembly by converting discrete solid-solid contacts into continuous, intimate interfacial contacts. Xu et al. reported a halide-based deep eutectic solid electrolyte (DESE) synthesized via a straightforward ball-milling approach.^[83] Intermolecular interactions within the halide mixture drive eutectic formation, generating a range of morphologies and viscosities depending on the composition. Cryogenic characterization of the chemical and microstructural features revealed uniform dispersion of LiCl and LiF nanoparticles within the amorphous halide matrix, which enhances ionic mobility and facilitates rapid Li⁺ transport. The optimized DESE exhibits a low activation energy and achieves a room-temperature ionic conductivity of up to 16 mS cm^{-1} , among the highest values reported for solid electrolytes. When integrated with active materials in composite cathodes, the viscous DESE promotes the formation of ultradense

Table 2. Electrochemical performance of different gel-based SSE systems.

SSEs	Ionic conductivity [mS cm ⁻¹ @ 25°C]	Cathode	Performance [mAh g ⁻¹ @C@ 25°C @Cycle number]	Rate [mAh g ⁻¹ @C]	Reference
Li ₆ PS ₅ Cl-PEO/LiTFSI	1.02@60	LiFePO ₄	93.74@0.5@25@15	–	[58]
Li ₆ PS ₅ Cl/PFPE	0.34@25	–	–	–	[59]
Li ₃ PS ₄ -PEO	–	LiFePO ₄	143@1@60@1000	153.4@0.1	[61]
PEO-Al-LTZ	0.426@60	–	–	–	[62]
Li ₆ PS ₅ -ether-nitrile copolymer	0.104@25	NCM622	132.4@0.5@55@500	180.5@0.1	[64]
PEO-Li ₂ SnS ₄	0.0255@30	LiFePO ₄	141@0.1@25@65	77@0.5	[65]
Li ₆ PS ₅ Cl-PEO-CTMS-PET	0.75@25	LiFePO ₄	163.6@0.1@25@100	135.2@1	[66]
LPSCI-PEO/LATP	–	LiNi _{0.9} Co _{0.08} Mn _{0.02} O ₂	192.8@0.1@60@/	124.4@0.5	[67]
PEO/Li _{5.6} PS _{4.6} Cl _{1.4}	0.126@40	PTO	342.3@0.3@25@500	102@2	[68]
PE-Li ₃ PS ₄	0.0737@20	–	–	–	[69]
cPAN-LATP	2.56@25	NCM622	158.7@0.5@RT@500	87.3@2	[70]
PEO-LLZTO	0.13@25	LiFePO ₄	158.9@1@25@1000	–	[71]
EVA-Li ₁₀ GeP ₂ S ₁₂	–	S-EVA	1345.2@0.2@50@100	705@1	[72]
PEGDME-LiTFSI/LiFSI	–	LiNi _{0.85} Co _{0.1} Mn _{0.05} O ₂ @LNbO	166.5@0.1@60@100	–	[73]
Li ₇ P ₃ S ₁₁ -PPy@NCNT	123@25	Sulfur	1351@0.1@60@30	600@1	[76]
Li ₆ PS ₅ Cl-PAP	4.67@RT	Ni _{0.9} Co _{0.075} Mn _{0.025} O ₂	90@5@RT@2000	227.6@0.1	[77]
Li ₆ PS ₅ Cl-PDA@VGCF	–	LiNi _{0.8} Co _{0.15} Al _{0.05} O ₂	209@0.1@RT@100	–	[78]
PE-Li ₃ PS ₄	0.0172@20	–	–	–	[31]
Li _{5.5} PS _{4.5} Cl _{1.5} -PVCA	2.7@25	NCM622	173.5@0.1@RT@300	74.8@2	[80]
SHPUSB-Li ₇ P ₃ S ₁₁	1.51@60	NMC622	1.76Ah@0.5@30@350	–	[57]
Li ₁₀ GeP ₂ S ₁₂ -DMC-PVDF-HFP	2@25	–	–	–	[81]
Li ₆ PS ₅ Cl-GPE	0.41@25	NCM711	170@0.05@25@100	–	[82]
LPSCI-DESEs	16@25	–	–	–	[83]

electrode particles, delivering ionic conductivity significantly higher than conventional sulfide-based additive systems and underscoring its potential for high-performance ASSLIBs.

The incorporation of gel polymers into SSE systems is widely regarded as an effective strategy to mitigate interfacial resistance and improve both ion transport and mechanical compatibility. **Table 2** systematically compares various gel polymers combined with SSE and their corresponding electrochemical performance, including ionic conductivity, cathode selection, cycling stability, and rate capability. Overall, the introduction of gel polymers demonstrates significant advantages in optimizing interfacial chemistry and structure: on one hand, their flexible network structures can buffer mechanical stress at the electrode/electrolyte interface, preventing interfacial cracking caused by volume changes; on the other hand, gel systems often provide ion-rich pathways at the interface, reducing the accumulation of interfacial resistance and thereby effectively enhancing cycle life and rate performance. In contrast, gel polymers with poor compatibility may induce side reactions and interface instability, resulting in increased resistance and limited overall electrochemical performance. In general, rational design of gel polymer requires not only maintaining high ionic conductivity but also molecular-level regulation of polymer segment mobility, solvation environment, and chemical compatibility with sulfides to achieve a balance between interfacial stability and electrochemical activity. Despite the unique advantages of gel polymers in interfacial optimization, several challenges remain. First, the ionic conductivity of gel polymer is generally lower than that of inorganic SSE, and their ion migration capability under high current density or low-temperature conditions remains insufficient, limiting the high-power performance of full cells. Second, the chemical stability of the organic components in some gel polymer systems is relatively poor, making them prone to decomposition under high voltage or long-term cycling conditions, which leads to the formation of interfacial byproducts and accelerated resistance growth.

3. Conclusion and Outlook

The development of PSCSEs represents a promising direction for next-generation ASSLIBs. By integrating the high ionic conductivity of sulfide ceramics with the flexibility and stability of polymer matrices, PSCSEs offer a compelling solution to the long-standing challenges of interface contact and mechanical stress. The works reviewed here demonstrate a wide range of effective strategies, from designing functional polymer binders and *in situ* formed interlayers to engineering novel composite structures. We have seen how specific binders like ionomers, spandex, PVDF-CTFE, and Li-doped Nafion can improve inter-particle adhesion, reduce interfacial resistance, and provide mechanical resilience to accommodate volume changes. The role of *in situ* polymerization and advanced characterization techniques like *in situ* XPS and transparent cell microscopy has been crucial in unraveling the complex interfacial reactions and dendrite growth mechanisms, paving the way for targeted mitigation strategies.

However, despite these remarkable advances, several challenges must be overcome to enable the widespread commercialization of PSCSE-based ASSLIBs. The high sensitivity of sulfide electrolytes to ambient moisture and oxygen remains a major manufacturing hurdle, leading to low production yields and requiring expensive dry-room facilities. A deeper understanding of the dynamic evolution of the solid-solid interfaces under long-term cycling is needed, as current models are often static and fail to predict performance degradation accurately. Furthermore, the absence of predictive multiphysics models hinders the rational design of new materials and cell architectures, often requiring extensive trial-and-error experimentation.

Looking ahead, we identify several key research directions that merit focused attention. First, artificial intelligence (AI) and machine learning (ML) can be leveraged for high-throughput materials screening and performance prediction, with the specific goal of establishing predictive models for PSCSE polymer/sulfide formulations that simultaneously optimize ionic conductivity, interfacial stability, and cycle life. Strategies include constructing a structure-property database and training ML models with combined MD simulations and experimental data, enabling the identification of potential high-performance materials within weeks, which can shorten the R&D cycle by 5–10 times compared to traditional trial-and-error approaches. Second, the development of advanced real-time, *in situ* characterization techniques to monitor buried interfaces in ASSLIBs is crucial. The technical objective is to capture the kinetics of interfacial reactions, dendrite initiation, and SEI/CEI layer evolution. Strategies involve integrating multiscale and multimodal methods such as *in situ* XPS, *in situ* TEM/SEM, and transparent cell microscopy to achieve full-time resolution of interface dynamics. This approach not only validates the performance of new materials but also provides precise design guidance for interface engineering, thereby reducing interfacial failure risks and extending cycle life. Finally, focusing on modular integration strategies that combine optimal materials with scalable manufacturing processes is critical for translating laboratory research into commercial production. The technical objectives focus on enabling continuous dry coating and roll-to-roll fabrication without compromising electrolyte/electrode uniformity or interfacial integrity. Low-temperature dry coating combined with roll-to-roll production could serve as a viable strategy, targeting material costs below \$50 m⁻² and production throughput of 50–100 m² h⁻¹. These capabilities stem from the polymeric components in PSCSEs, which provide the required mechanical flexibility and processability. Compared to wet processes, dry processing significantly reduces solvent costs and waste treatment, while roll-to-roll production offers high scalability suitable for large-area battery sheet fabrication, meeting industrial demands. By addressing these challenges, the PSCSE platform is poised to enable a new era of high-performance, ultrasafe ASSLIBs.

Acknowledgements

Y.Z. and Y.Y. contributed equally to this work. We thank the financial support from the National Natural Science Foundation of China

(52177218 and 52406067), the Shenzhen Science and Technology Program (JCYJ20230807153607017), and the Guangdong Basic and Applied Basic Research Foundation (2025A1515010387 and 2023A1515110139).

Conflict of Interest

The authors declare no conflict of interest.

Data Availability Statement

The data that support the findings of this study are available from the corresponding author upon reasonable request.

Keywords: all-solid-state lithium-ion batteries · polymer matrix · sulfide-based solid electrolytes

- [1] H. Du, Y. Wang, Y. Kang, Y. Zhao, Y. Tian, X. Wang, Y. Tan, Z. Liang, J. Wozny, T. Li, *Adv. Mater.* **2024**, *36*, 2401482.
- [2] C. Weng, M. Qiu, B. Wang, J. Yang, W. Mai, L. Pan, S. Huang, J. Li, *Angew. Chem. Int. Ed.* **2025**, *64*, e202419539.
- [3] J. Cheng, N.-X. Ci, H.-Q. Zhang, Z. Zeng, X. Zhou, Y.-Y. Li, H.-J. Qiu, W. Zhai, D.-D. Gao, L.-J. Ci, *Rare Met.* **2025**, *44*, 961.
- [4] S. Chen, Q. Peng, Z. Wei, Y. Li, Y. Yue, Y. Zhang, W. Zeng, K. Jin, L. Jiang, Q. Wang, *Energy Storage Mater.* **2024**, *70*, 103481.
- [5] Y. Liu, S. Lu, Z. Wang, J. Xu, S. Weng, J. Xue, H. Tu, F. Zhang, L. Liu, Y. Gao, *Adv. Funct. Mater.* **2024**, *34*, 2312295.
- [6] S. Zhang, S. Wu, J. Hwang, K. Matsumoto, R. Hagiwara, *J. Am. Chem. Soc.* **2024**, *146*, 8352.
- [7] Y. Lin, L. G. Somerville, R. Rashid, R. I. Ledesma, J. H. Kang, A. R. Kavanagh, J. S. Packard, C. H. Scrudger, A. L. Durgin, V. I. Yamakov, *Small* **2025**, *21*, 2409536.
- [8] N. Zhang, Z.-C. Lv, X.-Q. Chen, P.-F. Wang, Z.-L. Liu, J. Shu, T.-F. Yi, *J. Power Sources* **2025**, *644*, 237150.
- [9] C. Yang, Z. Jiang, X. Chen, W. Luo, T. Zhou, J. Yang, *Chem. Commun.* **2024**, *60*, 10245.
- [10] L. Devaraj, S. V. Thummalapalli, N. Fonseca, H. Nazir, K. Song, A. M. Kannan, *Mater. Today Sustainability* **2024**, *25*, 100614.
- [11] Y. Zhang, J.-H. Li, M. Ge, Y.-H. Huang, H.-H. Xu, *Rare Met.* **2024**, *43*, 5625.
- [12] S. Li, Z. Yang, S.-B. Wang, M. Ye, H. He, X. Zhang, C.-W. Nan, S. Wang, *Commun. Mater.* **2024**, *5*, 44.
- [13] X. Zhu, L. Wang, Z. Bai, J. Lu, T. Wu, *Nano Micro Lett.* **2023**, *15*, 75.
- [14] Q. Sun, G. Zeng, X. Xu, J. Li, J. J. Biendicho, S. Wang, Y. Tian, L. Ci, A. Cabot, *Adv. Energy Mater.* **2024**, *14*, 2402048.
- [15] Z. L. Dong, Y. Yuan, V. Martins, E. Jin, Y. Gan, X. Lin, Y. Gao, X. Hao, Y. Guan, J. Fu, *Nano Energy* **2024**, *128*, 109871.
- [16] T. Lu, S. Meng, M. Liu, *J. Mater. Chem. A* **2024**, *12*, 3954.
- [17] Y. Li, C. Kim, Y. Cho, A. L. Musgrave, G. D. Parker, Y.-F. Su, R. L. Sacci, X.-Y. Yu, T. Zawodzinski, J. Nanda, *Energy Storage Mater.* **2025**, *80*, 104385.
- [18] H. Liu, Y. Liang, C. Wang, D. Li, X. Yan, C. W. Nan, L. Z. Fan, *Adv. Mater.* **2023**, *35*, 2206013.
- [19] X. Randrema, I. L. Mifban, M. Soler, I. Profatilova, M. Berthault, R. Ramos, J. Lavie, E. De Vito, L. Blanc, S. Diry, *Batteries Supercaps* **2024**, *7*, e202300380.
- [20] J. Kim, W. Choi, S. J. Hwang, D. W. Kim, *Energy Environ. Mater.* **2024**, *7*, e12776.
- [21] H. Kim, M. J. Kim, M. S. Shin, H. N. Choi, I. Belharouak, Y. K. Sun, *Adv. Energy Mater.* **2025**, *15*, 2500867.
- [22] J.-C. Wang, W.-J. Zhou, N. Zhang, P.-F. Wang, T.-F. Yi, *Energy Fuels* **2024**, *38*, 18395.
- [23] P.-J. Lin, C.-H. Liao, S.-C. Yeh, Y.-C. Tseng, F.-C. Chang, W.-C. Chen, R.-J. Jeng, N.-L. Wu, C.-C. Chueh, *ACS Sustainable Chem. Eng.* **2023**, *11*, 10191.
- [24] Y.-H. Lee, D.-H. Kim, J.-M. Yoon, I.-C. Choi, J.-H. Choi, K.-J. Jeon, Y.-C. Ha, C.-M. Park, *Joule* **2024**, *8*, 2777.
- [25] M. Muzakir, K. Manickavasakam, E. J. Cheng, F. Yang, Z. Wang, H. Li, X. Zhang, J. Qin, *J. Mater. Chem. A* **2025**, *13*, 73.
- [26] S. Liu, L. Zhou, T. Zhong, X. Wu, K. Neyts, *Adv. Energy Mater.* **2024**, *14*, 2403602.
- [27] P. Wang, J.-H. Liu, W. Cui, X. Li, Z. Li, Y. Wan, J. Zhang, Y.-Z. Long, *J. Mater. Chem. A* **2023**, *11*, 16539.
- [28] Y. Yang, Q. Wu, D. Wang, C. Ma, Z. Chen, Q. Su, C. Zhu, C. Li, *J. Membrane Sci.* **2020**, *612*, 118424.
- [29] D. Lin, P. Y. Yuen, Y. Liu, W. Liu, N. Liu, R. H. Dauskardt, Y. Cui, *Adv. Mater.* **2018**, *30*, 1802661.
- [30] X. Chen, X. Li, L. Luo, S. He, J. Chen, Y. Liu, H. Pan, Y. Song, R. Hu, *Adv. Energy Mater.* **2023**, *13*, 202301230.
- [31] P. Mirmira, C. Fuschi, Z. Umlauf, P. Ma, E. S. Doyle, M. C. Vu, C. V. Amanchukwu, *J. Electrochem. Soc.* **2024**, *171*, 030508.
- [32] X. Chen, X. Li, L. Luo, S. He, J. Chen, Y. Liu, H. Pan, Y. Song, R. Hu, *Adv. Energy Mater.* **2023**, *13*, 2301230.
- [33] T. Schmaltz, F. Hartmann, T. Wicke, L. Weymann, C. Neef, J. Janek, *Adv. Energy Mater.* **2023**, *13*, 2301886.
- [34] P. Mirmira, E. S. Doyle, P. Ma, A. Garcia, Z. Umlauf, M. C. Vu, C. V. Amanchukwu, *Chem. Mater.* **2025**, *37*, 1069.
- [35] A. Bhargav, H. Y. Asl, A. Manthiram, *J. Mater. Chem. A* **2023**, *11*, 9772.
- [36] R. Deng, T. He, *Energies* **2023**, *16*, 4549.
- [37] X. Yi, Y. Yang, K. Xiao, S. Zhang, B. Wang, N. Wu, B. Cao, K. Zhou, X. Zhao, K. W. Leong, *Adv. Energy Mater.* **2025**, *15*, 2404973.
- [38] S. B. Hong, Y. J. Lee, U. H. Kim, C. Bak, Y. M. Lee, W. Cho, H. J. Hah, Y. K. Sun, D. W. Kim, *ACS Energy Lett.* **2022**, *7*, 1092.
- [39] J. Oh, S. H. Choi, B. Chang, J. Lee, T. Lee, N. Lee, H. Kim, Y. Kim, G. Im, S. Lee, *ACS Energy Lett.* **2022**, *7*, 1374.
- [40] S. Liu, L. Zhou, J. Han, K. Wen, S. Guan, C. Xue, Z. Zhang, B. Xu, Y. Lin, Y. Shen, *Adv. Energy Mater.* **2022**, *12*, 2200660.
- [41] K. T. Kim, T. Y. Kwon, Y. B. Song, S.-M. Kim, S. C. Byun, H.-S. Min, S. H. Kim, Y. S. Jung, *Chem. Eng. J.* **2022**, *450*, 138047.
- [42] Y. Ren, N. Hortance, K. B. Hatzell, *J. Electrochem. Soc.* **2022**, *169*, 060503.
- [43] Y.-J. Lee, S.-B. Hong, D.-W. Kim, *J. Ind. Eng. Chem.* **2023**, *122*, 341.
- [44] D. Li, H. Liu, C. Wang, C. Yan, Q. Zhang, C. W. Nan, L. Z. Fan, *Adv. Funct. Mater.* **2024**, *34*, 2315555.
- [45] W.-H. Jeong, H. Kim, S. Kansara, S. Lee, M. Agostini, K. Kim, J.-Y. Hwang, Y.-C. Jung, *Energy Storage Mater.* **2024**, *73*, 103855.
- [46] Y.-H. Jo, Y.-J. Lee, D.-W. Kim, *J. Electrochem. Soc.* **2024**, *171*, 100525.
- [47] B.-S. Kang, S.-H. Jeon, S.-J. Park, Y.-W. Song, J. Lim, Y. Hong, M.-Y. Kim, H.-S. Kim, *J. Electrochem. Soc.* **2024**, *171*, 090520.
- [48] H. Liu, W. Jiang, W. Chen, Q. Lin, S. Ren, Y. Su, R. Tong, Y. Zhang, *J. Mater. Chem. A* **2024**, *12*, 3575.
- [49] Z. Li, S. Zheng, B. Zhang, *J. Mater. Chem. A* **2024**, *12*, 28139.
- [50] J. Cha, S. Kim, U. T. Nakate, D.-W. Kim, *J. Power Sources* **2024**, *613*, 234914.
- [51] Y. Song, H. Qu, Z. Lao, X. Xiao, G. Lu, Y. Song, L. Nie, J. Wang, J. Yang, Y. Zhu, *Adv. Mater.* **2025**, *37*, 2419271.
- [52] M. Li, K. Pan, D. Huang, J. Wu, Z. Li, Y. Dou, Z. Zhang, Z. Zhou, *Adv. Sci.* **2025**, *12*, e03664.
- [53] J. Choi, C. Bak, J. Y. Kim, D. O. Shin, S. H. Kang, Y. M. Lee, Y.-G. Lee, *J. Energy Chem.* **2025**, *105*, 514.
- [54] A. Morchhale, Z. Tang, C. Yu, R. Farahati, J.-H. Kim, *Curr. Opin. Electrochem.* **2023**, *39*, 101251.
- [55] H. Xu, Y. Su, C. Zheng, Y. Wang, Y. Tong, Z. Yang, J. Hu, *Chin. Chem. Lett.* **2024**, *35*, 109173.
- [56] F. Yi, Z. Li, Q. Guo, F. Luo, P. Hu, Z. Liu, *J. Power Sources* **2023**, *580*, 233388.
- [57] X. Wang, S. He, Z. Hu, H. Xu, L. Pan, J. Li, *Rare Met.* **2025**, *44*, 7159.
- [58] C. Zou, L. Yang, K. Luo, L. Liu, X. Tao, L. Yi, X. Liu, Z. Luo, X. Wang, *ACS Appl. Energy Mater.* **2022**, *5*, 2356.
- [59] Y. Kamikawa, K. Amezawa, *ACS Appl. Energy Mater.* **2022**, *5*, 13243.
- [60] Y. Su, X. Zhang, C. Du, Y. Luo, J. Chen, J. Yan, D. Zhu, L. Geng, S. Liu, J. Zhao, *Small* **2022**, *18*, 2202069.
- [61] J. Xu, J. Li, Y. Li, M. Yang, L. Chen, H. Li, F. Wu, *Adv. Mater.* **2022**, *34*, 2203281.
- [62] G. Polizos, M. Goswami, J. K. Keum, L. He, C. J. Jafta, J. Sharma, Y. Wang, L. T. Kearney, R. Tao, J. Li, *ACS Nano* **2024**, *18*, 2750.
- [63] P. Ghorbanzade, A. Pesce, M. Armand, K. Gómez, S. Devaraj, P. López-Aranguren, J. M. López del Amo, *Small Struct.* **2024**, *5*, 2400139.
- [64] H. Yuan, C. Tian, M. Song, W. Lin, T. Huang, A. Yu, *J. Energy Chem.* **2024**, *91*, 628.
- [65] L. Zheng, G. Ren, S. Wang, Y. Yang, *J. Electron. Mater.* **2024**, *53*, 7400.
- [66] S. Yuan, Y. Luo, X. Wang, C. Yao, K. Xia, J. Xiao, X. Fang, G. Jiang, J. Xiong, M. Fan, *J. Energy Storage* **2024**, *90*, 111853.

- [67] K. Xiao, P. Ren, X. Wang, H. Chen, Q. Zhou, *Mater. Lett.* **2024**, *362*, 136221.
- [68] M. P. Thorat, R. Ali, M. D. Singh, M. S. Khan, R. Bormon, T. Shibi, S. Verma, K. S. Nalwa, *Mater. Today Energy* **2025**, *49*, 101849.
- [69] P. Mirmira, C. Fuschi, W. Gillett, P. Ma, J. Zheng, Z. D. Hood, C. V. Amanchukwu, *ACS Appl. Energy Mater.* **2022**, *5*, 8900.
- [70] Y. Liang, H. Liu, G. Wang, C. Wang, D. Li, Y. Ni, L. Z. Fan, *Adv. Energy Mater.* **2022**, *12*, 2201555.
- [71] S. Ma, Z. Yu, L. Wang, P. Zuo, *Langmuir* **2024**, *40*, 9255.
- [72] X. Zhu, W. Jiang, L. Wang, J. Lu, *Adv. Energy Mater.* **2024**, *14*, 2304244.
- [73] H. Huo, M. Jiang, B. Mogwitz, J. Sann, Y. Yusim, T. T. Zuo, Y. Moryson, P. Minnemann, F. H. Richter, C. V. Singh, *Angew. Chem. Int. Ed.* **2023**, *62*, e202218044.
- [74] M. Zhang, W. Xie, M. Liu, S. Liu, W. Wang, Z. Jin, A. Wang, J. Qiu, P. Zhao, Z. Shi, *ACS Appl. Mater. Interfaces* **2023**, *16*, 1578.
- [75] H. Yuan, C. Tian, M. Song, W. Lin, T. Huang, A. Yu, *J. Power Sources* **2024**, *602*, 234366.
- [76] R. Ma, Y. Fan, Y. Jin, S. Pan, H. Zhong, Y. Luo, J. Gu, M. Luo, Y. Wu, W. Hu, *Adv. Energy Mater.* **2024**, *14*, 2304412.
- [77] Z. Wang, X. Shen, S. Chen, R. Qiao, B. Sun, J. Deng, J. Song, *Adv. Mater.* **2024**, *36*, 2405025.
- [78] T. H. L. Vuong, N. R. Mastoi, J. S. Nam, W. T. A. Ran, C. Ha, M.-S. Park, Y.-J. Kim, *Chem. Eng. J.* **2024**, *497*, 154534.
- [79] J. Gu, W. Hu, Y. Wu, F. Ren, Z. Liang, H. Zhong, X. Zheng, R. Ma, Y. Luo, X. Chen, *Chem. Mater.* **2024**, *36*, 4403.
- [80] H. Yuan, W. Lin, C. Tian, T. Huang, A. Yu, *Nano Energy* **2024**, *128*, 109835.
- [81] X. Wang, L. Ye, C.-W. Nan, X. Li, *ACS Appl. Mater. Interfaces* **2022**, *14*, 46627.
- [82] K.-S. Oh, J. E. Lee, Y.-H. Lee, Y.-S. Jeong, I. Kristanto, H.-S. Min, S.-M. Kim, Y. J. Hong, S. K. Kwak, S.-Y. Lee, *Nano Micro Lett.* **2023**, *15*, 179.
- [83] R. Xu, J. Yao, Z. Zhang, L. Li, Z. Wang, D. Song, X. Yan, C. Yu, L. Zhang, *Adv. Sci.* **2022**, *9*, 2204633.

Manuscript received: August 23, 2025

Revised manuscript received: October 11, 2025

Version of record online: